POLITECNICO DI TORINO
Repository ISTITUZIONALE

The Dirac paradox in 1+1 dimensions and its realization with spin-orbit coupled nanowires

Original
The Dirac paradox in 1+1 dimensions and its realization with spin-orbit coupled nanowires / Gogin, L., Rossi, L., Rossi, F., Dolcini, F.. - In: NEW JOURNAL OF PHYSICS. - ISSN 1367-2630. - STAMPA. - 24:5(2022), p. 053045. [10.1088/1367-2630/ac6cfe]

Availability:
This version is available at: 11583/2965836 since: 2022-06-07T07:09:16Z

Publisher:
IOP

Published
DOI:10.1088/1367-2630/ac6cfe

Terms of use:

This article is made available under terms and conditions as specified in the corresponding bibliographic description in the repository

Publisher copyright

(Article begins on next page)

25 November 2026

New Journal of Physics
The open access journal at the forefront of physics

Deutsche Physikalische Gesellschaft DPG IOP Institute of Physics

PAPER • OPEN ACCESS

The Dirac paradox in 1 + 1 dimensions and its realization with spin–orbit coupled nanowires

To cite this article: Leonid Gogin *et al* 2022 *New J. Phys.* **24** 053045

View the article online for updates and enhancements.

You may also like

- Integrable theories and generalized graded Maillet algebras
A Melikyan and G Weber
- The Riemann zeros as energy levels of a Dirac fermion in a potential built from the prime numbers in Rindler spacetime
Germán Sierra
- The zig-zag road to reality
S Colin and H M Wiseman

This content was downloaded from IP address 93.39.138.223 on 26/05/2022 at 06:10

New Journal of Physics
The open access journal at the forefront of physics

Deutsche Physikalische Gesellschaft DPG
IOP Institute of Physics

Published in partnership with: Deutsche Physikalische Gesellschaft and the Institute of Physics



OPEN ACCESS

RECEIVED
10 January 2022

REVISED
13 April 2022

ACCEPTED FOR PUBLICATION
5 May 2022

PUBLISHED
23 May 2022

Original content from this work may be used under the terms of the Creative Commons Attribution 4.0 licence.

Any further distribution of this work must maintain attribution to the author(s) and the title of the work, journal citation and DOI.



PAPER

The Dirac paradox in 1 + 1 dimensions and its realization with spin–orbit coupled nanowires

Leonid Gogin, Lorenzo Rossi*, Fausto Rossi and Fabrizio Dolcini

Dipartimento di Scienza Applicata e Tecnologia del Politecnico di Torino, I-10129 Torino, Italy
* Author to whom any correspondence should be addressed.

E-mail: lorenzo.rossi@polito.it

Keywords: massless Dirac fermions, spin–orbit nanowires, helical states, scattering matrix formalism, heterojunctions

Abstract

At the interface between two massless Dirac models with opposite helicity a paradoxical situation arises: a transversally impinging electron can seemingly neither be transmitted nor reflected, due to the locking between spin and momentum. Here we investigate this paradox in one spatial dimension where, differently from higher dimensional realizations, electrons cannot leak along the interface. We show that models involving only massless Dirac modes lead to either no solutions or to trivial solutions to the paradox, depending on how the helicity change across the interface is modeled. However, non trivial scattering solutions to the paradox are shown to exist when additional massive Dirac modes are taken into account. Although these modes carry no current for energies within their gap, their interface coupling with the massless modes can induce a finite and tunable transmission. Finally, we show that such massless + massive Dirac model can be realized in suitably gated spin–orbit coupled nanowires exposed to an external Zeeman field, where the transmission coefficient can be controlled electrically.

1. Introduction

Conventional semiconductor heterostructures are typically described, within the envelope function and effective mass approximations, by a Schrödinger Hamiltonian with a space dependent effective electron mass varying along the growth direction and accounting for the different effective masses of the component materials.

In the last two decades, however, it has been realized that in various materials such as graphene, topological insulators and Weyl semimetals, the dynamics of the conduction electrons is well captured, in physically relevant regimes, by a $(D+1)$-dimensional *massless* Dirac electron model [1–7], where D denotes the spatial dimension, and '+1' the time dimension. These discoveries have thus spurred the interest in the investigation of Dirac heterojunctions. Each massless Dirac cone is characterized by a given helicity of the electron eigenstates, i.e. a sign encoding the locking between the propagation direction and the orientation of a 'spin-like' degree of freedom, which can be a sublattice pseudospin, like in graphene, or the actual angular momentum in topological insulators. In particular, when a junction is formed between two Dirac materials with opposite helicity, a paradoxical situation emerges, as sketched in figure 1. A right-moving electron (blue line on the left-hand side) impinging transversally towards a spin-inactive interface can neither be transmitted nor be reflected, due to spin conservation. The Dirac paradox has been discussed in heterojunctions between two 3D topological insulators, whose surface states are governed by a 2D massless Dirac Hamiltonian. In such a case the surface electrons turn out to 'escape' the problem by leaking along the interface surface [8–11]. However, in a truly 1D realization of a Dirac model such way out to an extra dimension does not exist and the Dirac paradox becomes even more interesting. The challenging question is whether a solution in 1D exists and, if so, whether it can be realized in some physical system.

In this paper we investigate the Dirac paradox in 1D and address these problems. First, we show that, if the helicity change across the interface is accounted for by an inhomogeneous velocity profile, the paradox has no solution, in the sense that the continuity equation forbids the existence of scattering states and only

© 2022 The Author(s). Published by IOP Publishing Ltd on behalf of the Institute of Physics and Deutsche Physikalische Gesellschaft

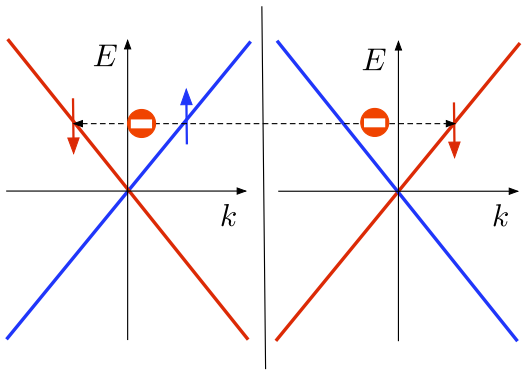


Figure 1. Schematic representation of the Dirac paradox emerging at a heterojunction between two massless Dirac models with opposite helicity. Blue and red lines describe spin-↑ and spin-↓ states, respectively. On the left-hand side of the junction, right-moving electrons are characterized by spin-↑ and left-moving electrons by spin-↓, while the opposite occurs on the right-hand side. A spin-↑ electron impinging from the left onto the interface can seemingly neither be transmitted nor reflected, due to spin conservation.

allows for eigenstates that involve electron injection from both sides of the junction, which carry a vanishing current. If, however, the interface directly introduces spin-rotation processes, the solution of the paradox is of course trivial and transmission is possible. We then investigate whether non-trivial solutions with proper scattering states and finite transmission exist without a spin-active interface. To this purpose, we propose an extended model involving both massless and massive Dirac modes. We show that, despite carrying no current for energies within their gap, the massive modes play a crucial role in inhomogeneous problems like the Dirac paradox. In particular, as will be discussed in details, scattering states describing a transmission from a spin-↑ incoming massless mode to a spin-↓ outgoing massless mode do exist, due to the interface coupling between massless and massive modes. Moreover, the resulting transmission coefficient is finite and tuneable.

We then discuss the possible realization of such extended model. While massless Dirac helical states have been proven to exist at the edges of quantum spin Hall systems [12–16], this implementation is not optimal for the Dirac paradox in 1D. Indeed, since these states flow at the boundaries of a 2D quantum well, an heterojunction between two such wells with opposite edge helicity would exhibit a linear interface, whereto electrons could leak, like in the case of heterojunctions between two 3D topological insulators mentioned above. However, a truly 1D implementation of helical states has been realized with spin–orbit coupled nanowires (NWs) exposed to a magnetic field [17–27], in the regime of spin–orbit energy much larger than the Zeeman energy [28–33].

So far, this remarkable discovery has been mostly exploited in the search for Majorana quasi-particles [20–27, 29, 30, 34–37]. However, further interesting research areas on NWs are fostered by the recent advances in gating techniques [38–43], which nowadays enable one to control the Rashba spin–orbit coupling (RSOC), both in magnitude [44–54] and sign [45, 55–57]. Because in a NW the helicity of the massless modes is determined by the sign of the RSOC, a NW with two differently gated regions can represent a truly 1D implementation of the Dirac paradox configuration. Notably, in such an inhomogeneous setup, the massless helical modes are not sufficient to describe the low energy physics, which turns out to be well captured by the massless + massive Dirac model we propose here, instead. The resulting conductance can be tuned electrically over a wide range of values.

Our paper is organized as follows. In section 2 we analyze the Dirac paradox with two different models involving only massless modes. Then, in section 3 we introduce a model with both massless and massive Dirac modes and show how this can yield a finite transmission coefficient depending on three parameters. Furthermore, in section 4 we show that this model can be implemented in a suitably designed setup involving spin–orbit coupled NWs. Finally, in section 5 we discuss our results and draw our conclusions.

2. Massless Dirac heterojunctions

Let us thus consider a junction connecting two 1 + 1 dimensional massless Dirac models

$$\hat{\mathcal{H}}_{\mathrm{L/R}} = v_{\mathrm{L/R}} \int \hat{\Psi}^{\dagger}(x)\sigma_z p_x \hat{\Psi}(x)\,\mathrm{d}x, \tag{1}$$

where $\hat{\mathcal{H}}_{\rm L}$ and $\hat{\mathcal{H}}_{\rm R}$ denote the Hamiltonians on the left and on the right side of the interface region, respectively, $\hat{\Psi} = (\hat{\Psi}_\uparrow, \hat{\Psi}_\downarrow)^{\rm T}$ is the 2×1 electron spinor field operator, $p_x = -{\rm i}\hbar\partial_x$ is the momentum operator, and σ_z is a Pauli matrix in spin space. Finally $v_{\rm L/R}$ denotes the Fermi velocity. When $v_{\rm R}$ and $v_{\rm L}$ have opposite signs, the helicity changes across the interface and the Dirac paradox emerges. The answer to the paradox, if any, heavily depends on how the crossover from $\hat{\mathcal{H}}_{\rm L}$ to $\hat{\mathcal{H}}_{\rm R}$ occurs, as we shall discuss here below considering different models.

2.1. Model 1: velocity sign change

The most straightforward way to implement the crossover from $\hat{\mathcal{H}}_{\rm L}$ to $\hat{\mathcal{H}}_{\rm R}$ is to assume that the entire system is characterized by an inhomogeneous velocity $v(x)$, varying from $v_{\rm L}$ to $v_{\rm R}$ over a certain crossover length λ. Since the momentum operator p_x does not commute with an inhomogeneous velocity profile $v(x)$, a quite natural approach is to replace their product $p_x v$ by a half of their anticommutator, obtaining the following Hamiltonian

$$\hat{\mathcal{H}} = \int \hat{\Psi}^\dagger(x)\sigma_z \frac{\{v(x), p_x\}}{2} \hat{\Psi}(x){\rm d}x. \tag{2}$$

The current operator associated to equation (2) is

$$\hat{J}(x) = ev(x)\hat{\Psi}^\dagger(x)\sigma_z\hat{\Psi}(x), \tag{3}$$

with e denoting the electron charge, whereas the Heisenberg equation dictated by Hamiltonian (2) reads

$$\partial_t\hat{\Psi} = -\sigma_z\left(v(x)\partial_x\hat{\Psi} + \frac{\partial_x v}{2}\hat{\Psi}\right). \tag{4}$$

Looking for stationary solutions $\hat{\Psi}(x,t) = \hat{\Psi}_E(x){\rm e}^{-{\rm i}Et/\hbar}$ and multiplying equation (4) by σ_z on the left, the equation reduces to

$$\partial_x\hat{\Psi} = v^{-1}(x)\left(-\frac{\partial_x v}{2}\sigma_0 + {\rm i}\frac{E}{\hbar}\sigma_z\right)\hat{\Psi}, \tag{5}$$

whose formal solution is

$$\hat{\Psi}_E(x) = \exp\left[-\frac{1}{2}\int_{x_{\rm R}}^{x}\frac{\partial_x v}{v(x')}{\rm d}x'\right] \times \exp\left[{\rm i}E\sigma_z\int_{x_{\rm R}}^{x}\frac{{\rm d}x'}{\hbar v(x')}\right]\hat{\Psi}_E(x_{\rm R}), \tag{6}$$

where $x_{\rm R}$ is some arbitrary reference space point. One can now exploit $\partial_x \ln|v(x)| = \partial_x v/v(x)$, denote $k_E(x) = E/\hbar v(x)$ and write

$$\hat{\Psi}_E(x_{\rm R}) = \frac{u}{\sqrt{2\pi\hbar|v(x_{\rm R})|}}\hat{a}_E, \tag{7}$$

where u is a position-independent 2×1 spinor and $\hat{a}_E$ the related energy-E mode operator fulfilling $\{a_E, a^\dagger_{E'}\} = \delta(E - E')$. At each energy E there are thus two independent solutions, corresponding to two mutually orthogonal choices for the spinor u. Then, equation (6) takes the form

$$\hat{\Psi}_E(x) = \frac{1}{\sqrt{2\pi\hbar|v(x)|}}{\rm e}^{{\rm i}\sigma_z\int_{x_{\rm R}}^{x}k_E(x'){\rm d}x'}\,u\,\hat{a}_E, \tag{8}$$

which straightforwardly implies that at any space point x, including possible discontinuity points of $v(x)$, the following boundary condition holds

$$\sqrt{|v(x^+)|}\hat{\Psi}_E(x^+) = \sqrt{|v(x^-)|}\hat{\Psi}_E(x^-), \tag{9}$$

where $x^\pm = x \pm \varepsilon$ with $\varepsilon \to 0$.

If $v(x)$ varies in magnitude from $v_{\rm L}$ to $v_{\rm R}$ while preserving a (say) positive sign, $v(x) = |v(x)|$, the Hamiltonian (2) can equivalently be rewritten as

$$\hat{\mathcal{H}} = \int \hat{\Psi}^\dagger(x)\sigma_z\sqrt{v(x)}\left[p_x\sqrt{v(x)}\right]\hat{\Psi}(x){\rm d}x. \tag{10}$$

In this case, one finds that the transmission coefficient is always 1, regardless of the specific values of $v_{\rm L}, v_{\rm R} > 0$, as discussed in reference [58].

If, however, $v(x)$ vanishes at some point x_0, like in the Dirac paradox, the problem becomes more subtle. Indeed in such case the energy dependent phase factor involving $k_E(x)$ in the solution equation (8) is well

defined only if $v(x)$ vanishes as $|v(x)| = O(|x - x_0|^\alpha)$ with $0 < \alpha < 1$. Moreover the solution diverges as $\sim 1/\sqrt{|v(x)|}$ for $x \to x_0$. Yet, in view of the condition (9), the current in equation (3) is finite. Denoting by $\hat{J}_E^\pm \doteq \hat{J}_E(x_0^\pm)$ the current operator for a stationary solution at energy E at the two sides of the point x_0 of vanishing velocity, one straightforwardly finds from equation (9) that $\hat{J}_E^+ = -\hat{J}_E^-$. For stationary solutions, however, the continuity equation requires the expectation value of the current to be continuous and independent of the position. The only possibility is that no current flows through the system, $\langle \hat{J}_E(x) \rangle \equiv 0 \ \forall \ x$, implying that the spinor u appearing in equation (8) *must be* chosen to have vanishing spin along z, i.e. $u^\dagger \sigma_z u = 0$. Up to an overall dimensional coefficient, two independent choices are $u_+ = (1, \mathrm{e}^{\mathrm{i}\phi})^\mathrm{T}/\sqrt{2}$ and $u_- = (\mathrm{e}^{-\mathrm{i}\phi}, -1)^\mathrm{T}/\sqrt{2}$, where ϕ is an arbitrary phase.

As an illustrative example, consider for instance the spatially odd profile $v(x) = -v_\mathrm{F}\,\mathrm{sgn}(x)\tanh^\alpha(|x|/\lambda)$, which describes a velocity sign change from $v_\mathrm{L} = +v_\mathrm{F}$ to $v_\mathrm{R} = -v_\mathrm{F}$ across the interface located at $x_0 = 0$, occurring over a lengthscale λ and with an exponent $0 < \alpha < 1$. It is straightforward to prove that the solution (8) is spatially even. Explicitly, choosing e.g. $x_\mathrm{R} = -4\lambda$ as a reference point and taking the phase $\phi = 0$ in the above spinors u, one finds $k_E(x) \simeq -E\,\mathrm{sgn}(x)/\hbar v_\mathrm{F}$ for $|x| \gg \lambda$. The two physically correct solutions of the Heisenberg equation (4) then read

$$\hat{\Psi}_\pm(x,t) = \int \frac{\mathrm{d}E}{\sqrt{2\pi\hbar v_\mathrm{F}}} \psi_{E\pm}(x)\,\mathrm{e}^{-\mathrm{i}Et/\hbar}\,\hat{a}_{E\pm}, \tag{11}$$

where the wavefunctions $\psi_{E\pm}$ for $|x| \gg \lambda$ take the form

$$\psi_{E\pm}(x) = \frac{\mathrm{e}^{-\mathrm{i}E|x|/\hbar v_\mathrm{F}}}{\sqrt{2}} \begin{pmatrix} 1 \\ 0 \end{pmatrix} \pm \frac{\mathrm{e}^{+\mathrm{i}E|x|/\hbar v_\mathrm{F}}}{\sqrt{2}} \begin{pmatrix} 0 \\ 1 \end{pmatrix}. \tag{12}$$

These solutions fulfill the continuity equation by carrying a vanishing current (see equation (3)). Note that the spatially even wavefunctions in equation (12) involve incoming waves from *both* sides and cannot be scattering state solutions. Moreover, any attempt to construct scattering states by their linear combinations would fail and would also violate the continuity equation.

In summary, the answer to the Dirac paradox provided by model 1 is that, when v_L and v_R have opposite signs, it is impossible to construct scattering state solutions that respect the continuity equation. The transmission coefficient cannot be properly defined. Physically correct solutions must necessarily involve incoming waves from both sides and carry no current, regardless of the specific magnitudes of $|v_\mathrm{L}|$ and $|v_\mathrm{R}|$. We conclude this section by noticing that the model 1 only involves the σ_z-component of spin (see equation (2)), and the space-dependent $v(x)$ changes magnitude and sign of such component. In this respect, the model is purely scalar.

2.2. Model 2: spin-active interface

The second model to approach the Dirac paradox is described by the Hamiltonian

$$\hat{\mathcal{H}} = v_F \int \hat{\Psi}^\dagger(x) \left(\mathrm{e}^{-\mathrm{i}\theta(x)\sigma_x/2} p_x \sigma_z\, \mathrm{e}^{+\mathrm{i}\theta(x)\sigma_x/2} \right) \hat{\Psi}(x)\,\mathrm{d}x, \tag{13}$$

where the helicity changes sign through a counter-clockwise rotation of the σ_z spin around the x-axis by a space-dependent angle $\theta(x)$ varying from $\theta_\mathrm{L} = 0$ to $\theta_\mathrm{R} = \pi$, over a certain crossover length. Thus, differently from the purely scalar model (2), the model (13) exploits the full SU(2) spin structure and Hamiltonian terms at two different points do not commute in general. The current operator related to the Hamiltonian (13) is

$$\begin{aligned} \hat{J}(x) &= e v_\mathrm{F} \hat{\Psi}^\dagger(x) \left(\mathrm{e}^{-\mathrm{i}\theta(x)\sigma_x/2} \sigma_z\, \mathrm{e}^{+\mathrm{i}\theta(x)\sigma_x/2} \right) \hat{\Psi}(x) \\ &= e v_F \hat{\Psi}^\dagger(x) \left[\sigma_z\, \cos\,\theta(x) - \sigma_y\, \sin\,\theta(x) \right] \hat{\Psi}(x). \end{aligned} \tag{14}$$

Integrating the Heisenberg equation for the field operator

$$\partial_x \left(\mathrm{e}^{\mathrm{i}\theta(x)\sigma_x/2} \hat{\Psi}(x) \right) = -\frac{\sigma_z}{v_F} \mathrm{e}^{\mathrm{i}\theta(x)\sigma_x/2} \partial_t \hat{\Psi}(x) \tag{15}$$

around any point x, including possible discontinuity points of $\theta(x)$, the following boundary condition is found

$$\mathrm{e}^{\mathrm{i}\theta(x^+)\sigma_x/2} \hat{\Psi}(x^+) = \mathrm{e}^{\mathrm{i}\theta(x^-)\sigma_x/2} \hat{\Psi}(x^-), \tag{16}$$

which in turn straightforwardly implies the continuity of the current operator (14). In particular, for a step-like model $\theta(x<0)=0$ and $\theta(x>0)=\pi$ of an interface located at $x_0=0$, equation (16) reduces to

$$\begin{aligned}\hat{\Psi}_\uparrow(0^+) &= \mathrm{i}\hat{\Psi}_\downarrow(0^-)\\ \hat{\Psi}_\downarrow(0^+) &= \mathrm{i}\hat{\Psi}_\uparrow(0^-)\end{aligned} \tag{17}$$

and describes a spin-rotation process occurring at the interface. Differently from model 1, the Heisenberg equation (15) does admit scattering state solutions $\hat{\Psi}_{E,\pm}(x,t)=\exp[-\mathrm{i}Et/\hbar]\psi_{E\pm}(x)\hat{a}_{E,\pm}/\sqrt{2\pi\hbar v_\mathrm{F}}$, where $\hat{a}_{E,\pm}$ are the energy-E mode operators for scattering from the left (+) and from right (-), respectively, and $\psi_{E\pm}(x)$ are the related scattering wavefunctions. For instance, the scattering state from left is given by

$$\begin{aligned}\psi_{E+}(x<0) &= \begin{pmatrix}1\\0\end{pmatrix}\mathrm{e}^{\mathrm{i}Ex/\hbar v_\mathrm{F}}+r\begin{pmatrix}0\\1\end{pmatrix}\mathrm{e}^{-\mathrm{i}Ex/\hbar v_\mathrm{F}}\\ \psi_{E+}(x>0) &= t\begin{pmatrix}0\\1\end{pmatrix}\mathrm{e}^{\mathrm{i}Ex/\hbar v_\mathrm{F}}\end{aligned} \tag{18}$$

and, when inserted in equation (17), straightforwardly implies $r=0$ and $t=\mathrm{i}$, leading to a perfect transmission $T=|t|=1$.

In summary, model 2 trivially solves the Dirac paradox by simply introducing spin-rotation processes at the interface.

3. Dirac heterojunctions with massless and massive modes

So far, we have considered heterojunctions that purely involve Dirac massless modes and we have obtained two opposite answers to the Dirac paradox, depending on how the helicity change across the interface is modelled. Model 1, based on an inhomogeneous scalar velocity profile, implies that physical solutions necessarily involve injections from both sides of the junction and predicts no current flowing through the system, whereas model 2 'circumvents' the paradox by introducing a spin-active interface. In this section we propose a model that, *without* introducing any direct spin-rotation processes at the interface, leads to a non-vanishing transmission.

Suppose that, along with the massless propagating Dirac fermions illustrated in figure 1, the system is also characterized by massive Dirac fermions, as sketched by the green curves of figure 2. Specifically, the model we consider is

$$\begin{aligned}\hat{\mathcal{H}} = v_\mathrm{F}\int \hat{\Psi}^\dagger(x)U^\dagger(x)\tau_z\sigma_z p_x\left(U(x)\,\hat{\Psi}(x)\right)\,\mathrm{d}x+\\ -\frac{\Delta}{2}\int\hat{\Psi}^\dagger(x)(\tau_0-\tau_z)\sigma_x\,\hat{\Psi}(x)\,\mathrm{d}x,\end{aligned} \tag{19}$$

where $\hat{\Psi}=(\hat{\xi}_\uparrow,\hat{\xi}_\downarrow,\hat{\eta}_\uparrow,\hat{\eta}_\downarrow)^\mathrm{T}$, with $\hat{\xi}_\uparrow,\hat{\xi}_\downarrow$ and $\hat{\eta}_\uparrow,\hat{\eta}_\downarrow$ denoting the massless and massive fields, respectively. Here σ_0 and $\boldsymbol{\sigma}=(\sigma_x,\sigma_y,\sigma_z)$ denote the 2×2 identity matrix and Pauli matrices acting on the spin space, whereas τ_0 and $\boldsymbol{\tau}=(\tau_x,\tau_y,\tau_z)$ the corresponding quantities acting on the massless–massive degree of freedom, which we shall label as pseudospin. In the first term of equation (19) the 4×4 matrix $U(x)$ interpolates from U_L on the left of the interface to its value U_R on the right, where $U_{\mathrm{L/R}}$ are required to fulfill the following properties

$$U_\mathrm{L}^\dagger\tau_z\sigma_z U_\mathrm{L}=+\tau_z\sigma_z \tag{20}$$

$$U_\mathrm{R}^\dagger\tau_z\sigma_z U_\mathrm{R}=-\tau_z\sigma_z, \tag{21}$$

so that the $\hat{\xi}_\uparrow,\hat{\xi}_\downarrow$ modes have helicity $+1$ on the left of the interface and -1 on the right, just like in the Dirac paradox configuration of figure 1, whereas the opposite occurs for the $\hat{\eta}_\uparrow,\hat{\eta}_\downarrow$ modes. The simplest example of a $U(x)$-matrix fulfilling the conditions (20)-(21) is $U(x)=\exp[\mathrm{i}\theta(x)\tau_x\sigma_0/2]$, where $\theta(x)$ is a space-dependent angle describing a rotation in *pseudospin* space around τ_x from $\theta_\mathrm{L}=0$ to $\theta_\mathrm{R}=\pi$ and causing the helicity flip, just like the spin-active model (13) introduces a rotation in spin space. As we shall see below, there exists in fact a much broader set of possible choices for $U(x)$ that turn out to describe interesting and realistic cases. The second term in equation (19) describes the mass term for $\hat{\eta}_\uparrow$ and $\hat{\eta}_\downarrow$, and we shall be interested in the energy window $|E|<\Delta$ inside their gap, where these massive modes carry no current.

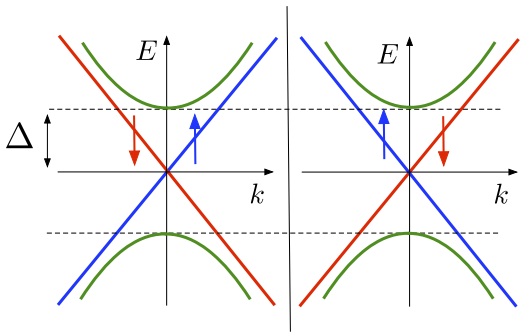


Figure 2. The band spectrum of the massless + massive Dirac model with opposite helicity across an interface. While blue and red curves denote the spectrum of the massless modes, as in figure 1, the green curves describe the spectrum of the massive modes, characterized by a gap 2Δ.

In view of equations (20) and (21), the current operator related to the Hamiltonian (19)

$$\hat{J}(x) = ev_{\mathrm{F}}\hat{\Psi}^{\dagger}(x)U^{\dagger}(x)\tau_z\sigma_z\, U(x)\hat{\Psi}(x) \tag{22}$$

takes opposite expressions $\hat{J}_{\mathrm{L/R}} = \pm ev_{\mathrm{F}}\hat{\Psi}^{\dagger}(x)\tau_z\sigma_z\,\hat{\Psi}(x)$ at the two sides of the interface. However, the boundary condition

$$U(x^{+})\hat{\Psi}(x^{+}) = U(x^{-})\hat{\Psi}(x^{-}), \tag{23}$$

obtained from integration of the Heisenberg equation around any point x, guarantees that the current is in fact continuous for any $U(x)$. In particular, adopting again a step-like model $U(x) = U_{\mathrm{L}}H(-x) + U_{\mathrm{R}}\mathrm{H}(x)$ for an interface located at $x_0 = 0$, with $H(x)$ denoting the Heaviside function, the field $\hat{\Psi}$ fulfills the interface boundary condition

$$\hat{\Psi}(0^{+}) = \mathsf{M}\,\hat{\Psi}(0^{-}), \tag{24}$$

where

$$\mathsf{M} = U_{\mathrm{R}}^{-1}U_{\mathrm{L}} \tag{25}$$

is the transfer matrix, which must fulfill

$$\mathsf{M}^{\dagger}\tau_z\sigma_z\mathsf{M} = -\tau_z\sigma_z \quad \text{(Requirement \#1)} \tag{26}$$

as a straightforward consequence of equations (20) and (21). Note that equation (24) implies that the field $\hat{\Psi}$ is discontinuous, as is customary for Dirac models in the presence of a $\delta(x)$-term, which in this case originates from $p_x U(x)$ term in the Hamiltonian (19).

Importantly, in order to avoid trivial solutions to the Dirac paradox like in model (13), we require that the model (19) does not directly introduce any spin-rotation process at the interface. This leads to impose another requirement on the transfer matrix equation (24), namely that M is diagonal in spin space, i.e.

$$\begin{matrix}\mathsf{M}\text{ must involve}\\ \text{only }\sigma_0\text{ and }\sigma_z\end{matrix} \quad \text{(Requirement \#2)}. \tag{27}$$

It can be shown (see appendix A for details) that the most general matrix fulfilling the requirements (26) and (27) has the following form in the $\tau\otimes\sigma$ basis

$$\mathsf{M} = \begin{pmatrix} \mathrm{i}\beta_{\uparrow}\,\mathrm{e}^{\mathrm{i}(\nu_{\uparrow}-\gamma_{\uparrow})} & 0 & (1-\mathrm{i}\beta_{\uparrow})\mathrm{e}^{\mathrm{i}(\nu_{\uparrow}+\chi_{\uparrow})} & 0 \\ 0 & \mathrm{i}\beta_{\downarrow}\mathrm{e}^{\mathrm{i}(\nu_{\downarrow}-\gamma_{\downarrow})} & 0 & (1-\mathrm{i}\beta_{\downarrow})\mathrm{e}^{\mathrm{i}(\nu_{\downarrow}+\chi_{\downarrow})} \\ (1+\mathrm{i}\beta_{\uparrow})\mathrm{e}^{\mathrm{i}(\nu_{\uparrow}-\chi_{\uparrow})} & 0 & -\mathrm{i}\beta_{\uparrow}\mathrm{e}^{\mathrm{i}(\nu_{\uparrow}+\gamma_{\uparrow})} & 0 \\ 0 & (1+\mathrm{i}\beta_{\downarrow})\mathrm{e}^{\mathrm{i}(\nu_{\downarrow}-\chi_{\downarrow})} & 0 & -\mathrm{i}\beta_{\downarrow}\mathrm{e}^{\mathrm{i}(\nu_{\downarrow}+\gamma_{\downarrow})} \end{pmatrix} \tag{28}$$

and depends on eight parameters, namely four real parameters $\chi_\sigma, \gamma_\sigma, \beta_\sigma, \nu_\sigma$ for each spin sector $\sigma = \uparrow, \downarrow$. The vanishing entries in equation (28) encode the decoupling of the two spin sectors dictated by equation (27).

3.1. Scattering states

Let us now focus on $E = 0$, i.e. on the middle of the massive energy gap, and build up scattering state solutions on both sides of the junction, namely

$$\hat{\Psi}(x<0) = \hat{a}_{\mathrm{L}\uparrow}\begin{pmatrix}1\\0\\0\\0\end{pmatrix}\mathrm{e}^{\mathrm{i}k_0 x} + \hat{b}_{\mathrm{L}\downarrow}\begin{pmatrix}0\\1\\0\\0\end{pmatrix}\mathrm{e}^{-\mathrm{i}k_0 x} + \frac{\hat{c}_{\mathrm{L}}}{\sqrt{2}}\begin{pmatrix}0\\0\\-\mathrm{i}\\1\end{pmatrix}\mathrm{e}^{\kappa_0 x} \tag{29}$$

and

$$\hat{\Psi}(x>0) = \hat{a}_{\mathrm{R}\uparrow}\begin{pmatrix}1\\0\\0\\0\end{pmatrix}\mathrm{e}^{-\mathrm{i}k_0 x} + \hat{b}_{\mathrm{R}\downarrow}\begin{pmatrix}0\\1\\0\\0\end{pmatrix}\mathrm{e}^{\mathrm{i}k_0 x} + \frac{\hat{c}_{\mathrm{R}}}{\sqrt{2}}\begin{pmatrix}0\\0\\-\mathrm{i}\\1\end{pmatrix}\mathrm{e}^{-\kappa_0 x} \tag{30}$$

where $k_0 = 0$, $\kappa_0 = \Delta/\hbar v_{\mathrm{F}}$. Here $\hat{a}_{\mathrm{L}\uparrow}$ and $\hat{a}_{\mathrm{R}\uparrow}$ are incoming operators describing a propagating mode impinging from the left (L) and from the right (R) of the interface, respectively, whereas $\hat{b}_{\mathrm{L}\downarrow}$ and $\hat{b}_{\mathrm{R}\downarrow}$ are outgoing operators for modes propagating to the left and to the right, respectively. Note that in the Dirac paradox configuration (see figure 2) incoming states and outgoing states have opposite spin, namely spin-↑ and spin-↓, respectively. Furthermore in equations (29) and (30) $\hat{c}_{\mathrm{L}}$ and $\hat{c}_{\mathrm{R}}$ describe evanescent modes on the left- and on the right-hand side of the interface. Importantly, because they are massive, their spinors have two non vanishing components and their spin points along y. Introducing equations (29) and (30) into equation (24) and using equation (28), one can write

$$\begin{pmatrix}\hat{b}_{\mathrm{L}\downarrow}\\ \hat{b}_{\mathrm{R}\downarrow}\\ \hat{c}_{\mathrm{L}}\\ \hat{c}_{\mathrm{R}}\end{pmatrix} = \begin{pmatrix}\mathsf{S}\\ \tilde{\mathsf{S}}\end{pmatrix}\begin{pmatrix}\hat{a}_{\mathrm{L}\uparrow}\\ \hat{a}_{\mathrm{R}\uparrow}\end{pmatrix}, \tag{31}$$

where S denotes the scattering matrix returning the outgoing propagating modes

$$\mathsf{S} = \frac{\mathrm{i}\,\mathrm{e}^{-\mathrm{i}\Delta\chi}}{(1-\mathrm{i}\beta_\uparrow)(1+\mathrm{i}\beta_\downarrow)} \times \begin{pmatrix} \mathrm{e}^{\mathrm{i}\Delta\nu} + \mathrm{e}^{-\mathrm{i}\Delta\gamma}\beta_\uparrow\beta_\downarrow & \mathrm{i}(\mathrm{e}^{\mathrm{i}(\gamma_\downarrow-\nu_\uparrow)}\beta_\downarrow - \mathrm{e}^{\mathrm{i}(\gamma_\uparrow-\nu_\downarrow)}\beta_\uparrow) \\ \mathrm{i}(\mathrm{e}^{\mathrm{i}(\nu_\uparrow-\gamma_\downarrow)}\beta_\downarrow - \mathrm{e}^{\mathrm{i}(\nu_\downarrow-\gamma_\uparrow)}\beta_\uparrow) & \mathrm{e}^{-\mathrm{i}\Delta\nu} + \mathrm{e}^{\mathrm{i}\Delta\gamma}\beta_\uparrow\beta_\downarrow \end{pmatrix} \tag{32}$$

with $\Delta\chi \doteq \chi_\uparrow - \chi_\downarrow$, $\Delta\nu \doteq \nu_\uparrow - \nu_\downarrow$ and $\Delta\gamma \doteq \gamma_\uparrow - \gamma_\downarrow$, whereas

$$\tilde{\mathsf{S}} = \frac{\sqrt{2}\,\mathrm{e}^{-\mathrm{i}\chi_\uparrow}}{1-\mathrm{i}\beta_\uparrow}\begin{pmatrix}\beta_\uparrow\,\mathrm{e}^{-\mathrm{i}\gamma_\uparrow} & \mathrm{i}\,\mathrm{e}^{-\mathrm{i}\nu_\uparrow}\\ \mathrm{i}\,e^{+\mathrm{i}\nu_\uparrow} & \beta_\uparrow\,\mathrm{e}^{\mathrm{i}\gamma_\uparrow}\end{pmatrix} \tag{33}$$

is the matrix yielding the evanescent modes.

In equation (31), setting $\hat{a}_{\mathrm{R}\uparrow} \to 0$ yields a scattering state with injection from left, while a scattering state with injection from right is obtained for $\hat{a}_{\mathrm{L}\uparrow} \to 0$. Thus, differently from model 1 in equation (2), the model in equation (19) does allow for scattering solutions. The transmission coefficient $T_0 = |t_0|^2$, obtained from the off-diagonal entries of the scattering matrix (32), reads

$$T_0 = \frac{\beta_\uparrow^2 + \beta_\downarrow^2 - 2\beta_\uparrow\beta_\downarrow\cos\varphi}{(1+\beta_\uparrow^2)(1+\beta_\downarrow^2)}, \tag{34}$$

and depends on the three parameters $\beta_\uparrow$, $\beta_\downarrow$ and $\varphi = \Delta\gamma + \Delta\nu$. To understand how the transmission between two propagating electronic states with oppositely oriented spins is possible, let us for instance set $\hat{a}_{\mathrm{R}\uparrow} \to 0$ in equation (31), which corresponds to a scattering process where a spin-↑ state incoming from the far left is transmitted into a spin-↓ state outgoing to the far right. By inspecting the spin spatial profile of equations (29) and (30), one observes that far away from the interface the total spin is mainly carried by the massless propagating states and is directed along the z-axis. However, near the interface, spin acquires also a component along y because of the presence of the massive states (third terms of equations (29) and (30)). Indeed the conservation of $S_z^{\mathrm{tot}} = \hbar\,\hat{\Psi}^\dagger\tau_0\sigma_z\hat{\Psi}/2$ is broken precisely by the mass in the Hamiltonian (19). Thus, when approaching the interface, the total spin *rotates* in the y–z plane, thereby allowing the transmission from a spin-↑ to a spin-↓ massless state. Note the essential difference with respect to model 2: there, the spin-rotation is induced *directly* on the massless modes by a spin-active interface (see

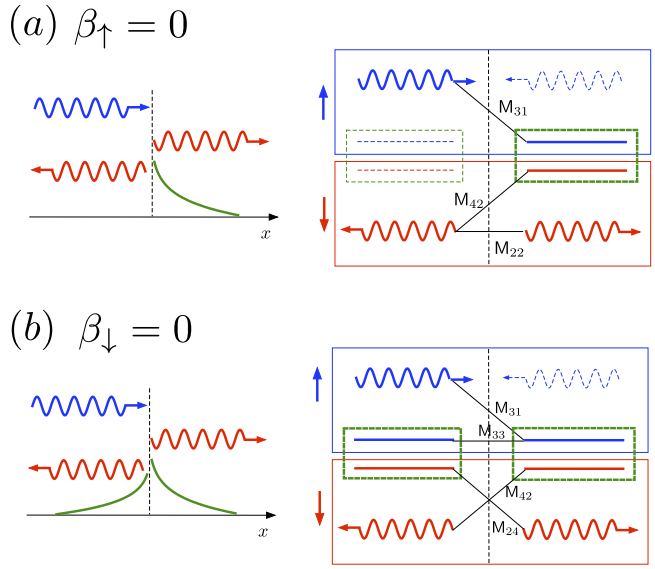


Figure 3. For each panel, the left-hand side sketches the scattering state wavefunction in the case of injection from the left, resulting from equations (31)–(33) for $\hat{a}_{R\uparrow} \to 0$. Blue and red wiggy lines describe spin-↑ and spin-↓ propagating massless states, respectively, whereas solid green lines describe the evanescent wave of the massive mode. The right-hand side of each panel is a graphical representation of equation (24), where black lines represent the transfer matrix entries connecting the non vanishing components of such scattering state. (a) The case with $\beta_\uparrow = 0$. The evanescent mode is present only on the right side of the interface. Here $\mathsf{M}_{31} = 1$, $M_{42} = 1 + \mathrm{i}\beta_\downarrow$ and $\mathsf{M}_{22} = \mathrm{i}\beta_\downarrow$. (b) The case with $\beta_\downarrow = 0$. In this case the evanescent modes are present on both sides of the junction. Here $\mathsf{M}_{31} = 1 + \mathrm{i}\beta_\uparrow$, $M_{33} = -\mathrm{i}\beta_\uparrow$ and $\mathsf{M}_{24} = \mathsf{M}_{42} = 1$. In all cases, despite the transfer matrix only connects states with the same spin, the presence of the evanescent modes of the massive field enables a spin-flip transmission between the propagating modes.

equation (13)), whereas here the transfer matrix in equations (24) and (28) is fully diagonal in spin (see equation (27)) and the spin rotation occurs *indirectly*, i.e. through the coupling between massless and massive modes localized at the interface.

To a more formal level, the process can be illustrated in terms of the transfer matrix as follows. Let us again consider for definiteness the scattering from left, i.e. $\hat{a}_{R\uparrow} \to 0$ in equation (31), and also set for simplicity all phases to zero ($\gamma_\sigma = \chi_\sigma = \nu_\sigma = 0$) in equations (28), (32) and (33). We first focus on the case $\beta_\uparrow = 0$, where the scattering state resulting from equations (31)–(33) is sketched on the left-hand side of figure 3(a): the blue (red) wiggy line describes the incoming spin-↑ state (outgoing spin-↓ states), while an evanescent wave (green solid line) is present only for $x > 0$. Its role is elucidated on the right-hand side of figure 3(a), which is a graphical representation of equation (24) where the non-vanishing components of such a scattering state are connected across the interface by the transfer matrix entries (black lines). When the massless spin-↑ state propagates towards the interface from the left, the transfer matrix equation (28) connects it through the entry $\mathsf{M}_{31} = 1$ to its massive evanescent partner with the same spin located across the interface, represented by a green dashed box, with the thick solid lines inside it denoting its two spin components. Because such a mode is massive, inside the gap it always exhibits *both* spin components (see third term in equation (30)). Thus, its spin-↓ component is also present and is connected through the transfer matrix entry $\mathsf{M}_{42} = 1 + \mathrm{i}\beta_\downarrow$ to its spin-↓ massless partner, which describes the reflected wave propagating to the left of the junction. Finally, the latter is also coupled, through the entry $\mathsf{M}_{22} = \mathrm{i}\beta_\downarrow$, to the massless spin-↓ state outgoing to the right of the junction. Thus, despite the interface connects only states with the same spin on the two sides, the presence of an evanescent massive mode exhibiting both spin components leads to an effective spin-flip transmission between massless modes.

Let us now consider the case $\beta_\downarrow = 0$. In this case the scattering state resulting from the solution equations (31)–(33) exhibits evanescent modes on both sides of the junction, as sketched in the left-hand side of figure 3(b). The scheme on the right-hand side of figure 3(b) illustrates the related equation (24). While the entry M_{31} is modified to $\mathsf{M}_{31} = 1 + \mathrm{i}\beta_\uparrow$, a connection $\mathsf{M}_{33} = -\mathrm{i}\beta_\uparrow$ opens up across the junction between the two spin-↑ components of the massive modes. In turn, their corresponding spin-↓ components are connected through the entries $\mathsf{M}_{24} = \mathsf{M}_{42} = 1$ to the spin-↓ massless modes across the junction, thereby inducing again spin-flipped reflection and transmission.

The general case, where both $\beta_\uparrow$ and $\beta_\downarrow$ are non vanishing, is a combination of the two elementary cases and yields the transmission coefficient (34). Note that in the limit where both $\beta_\uparrow \to 0$ and $\beta_\downarrow \to 0$, the transmission coefficient (34) vanishes. This can also be understood by realizing that in such limit the

transfer matrix (28) reduces to $\mathsf{M} = \tau_x\sigma_0$, yielding the boundary conditions

$$\begin{cases} \hat{\xi}_\sigma(0^+) = \hat{\eta}_\sigma(0^-) \\ \hat{\eta}_\sigma(0^+) = \hat{\xi}_\sigma(0^-) \end{cases} \quad \sigma = \uparrow, \downarrow, \tag{35}$$

so that e.g. a massless mode incoming from the left towards the interface is completely transformed into its massive evanescent mode partner across the interface (with the same spin), which carries no current.

In summary, although massive modes do not carry any current inside the gap, their presence is important in inhomogeneous problems because they may localize at the interfaces. In particular they are crucial in the Dirac paradox, for they provide an indirect coupling between the two spin channels that would be otherwise uncoupled by the interface transfer matrix. This leads to an effective spin-flip transmission of the massless propagating modes. Moreover, in contrast with the models 1 and 3 discussed in section 2, here the transmission coefficient is tunable from 0 to 1 through the three knobs $\beta_\uparrow, \beta_\downarrow$ and φ. This is one of the main results of our paper.

4. Spin–orbit coupled nanowires

In this section we shall show that the model presented in section 3 can be realized with spin–orbit coupled NWs, under suitable circumstances. First, we shall briefly recall how these systems, when exposed to an external magnetic field, can host helical states described by Dirac massless fermions, as well as gapped Dirac states. Then, focussing on energies inside the gap opened up by the magnetic field, we shall explicitly derive the effective low-energy model for these systems. Finally, we shall consider an inhomogeneous spin–orbit coupling profile that, in suitable regimes, realizes the Dirac paradox configuration involving both massless and massive modes, just like in the model proposed above.

4.1. The NW Hamiltonian and its low energy limit

We consider a ballistic single-channel semiconductor NW deposited on a substrate. For NWs like InSb or InAs, the structural inversion asymmetry can lead to quite strong RSOC [23, 44, 59–62], which can further be tuned with appropriate gating techniques. Furthermore we assume that a uniform magnetic field is applied parallel to the NW axis, denoted by x, while the substrate plane will be identified as x–z.

We shall adopt a widely used model to describe the NW [28–33], whose main ingredients are summarized here below, while details are reported in appendix B for the sake of completeness. The second-quantized NW Hamiltonian consists of three terms $\hat{\mathcal{H}}_{\rm NW} = \hat{\mathcal{H}}_{\rm kin} + \hat{\mathcal{H}}_{\rm R} + \hat{\mathcal{H}}_{\rm Z}$ and can be written as $\hat{\mathcal{H}}_{\rm NW} = \int \hat{\Phi}^\dagger(x) H_{\rm NW}(x) \hat{\Phi}(x) {\rm d}x$. Here $\hat{\Phi}(x) = (\hat{\Phi}_\uparrow(x),\ \hat{\Phi}_\downarrow(x))^{\rm T}$ is the electron spinor field, with $\uparrow, \downarrow$ corresponding to spin projections along z, and

$$H_{\rm NW}(x) = \frac{p_x^2}{2m^*}\sigma_0 - \frac{\alpha}{\hbar} p_x \sigma_z \ - h_x \sigma_x \tag{36}$$

contains the kinetic term characterized by an effective mass m^*, the Rashba term with a RSOC α, and the Zeeman term describing the coupling $h_x = g\mu_{\rm B} B_x/2$ with the external magnetic field $\mathbf{B} = (B_x, 0, 0)$, with $\mu_{\rm B}$ denoting the Bohr magneton and g the NW Landé factor. The model is characterized by two energy scales, namely the spin–orbit energy

$$E_{\rm SO} = \frac{m^* \alpha^2}{2\hbar^2}, \tag{37}$$

and the Zeeman energy

$$E_{\rm Z} = |h_x|. \tag{38}$$

For definiteness, we shall henceforth assume $h_x > 0$ and identify $h_x = E_{\rm Z}$. The spin–orbit wavevector

$$k_{\rm SO} = \frac{\sqrt{2m^* E_{\rm SO}}}{\hbar} = \frac{|\alpha| m^*}{\hbar^2}, \tag{39}$$

and the Zeeman wavevector

$$k_{\rm Z} = \sqrt{2m^* E_{\rm Z}}/\hbar \tag{40}$$

are the wavevectors associated to such energies. Diagonalizing the model in momentum space, one obtains a spectrum characterized by two energy bands separated at $k = 0$ by a gap $2E_{\rm Z}$ centered around the energy $E = 0$. Depending on the ratio of $E_{\rm Z}$ to $E_{\rm SO}$, the qualitative behavior of these bands is different. In fact, two regimes can be identified: (a) for $E_{\rm Z} > 2E_{\rm SO}$ (Zeeman-dominated regime) both bands have a minimum at $k = 0$ taking values $E_\pm^{\rm min} = \pm E_{\rm Z}$, whereas (b) for $E_{\rm Z} < 2E_{\rm SO}$ (Rashba-dominated regime) the upper band

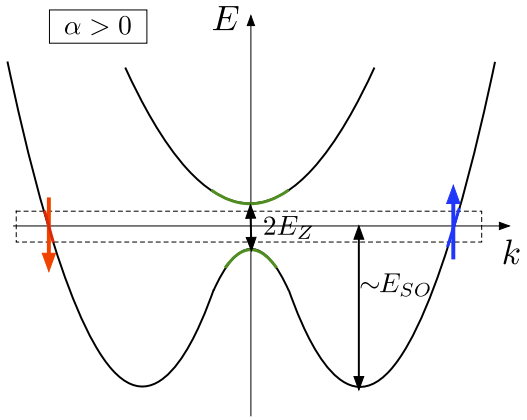


Figure 4. In the deep Rashba-dominated regime ($2E_{\rm SO} \gg E_{\rm Z}$) and for energies $|E| \ll E_{\rm Z}$, a NW exposed to an external magnetic field exhibits helical states near the Fermi points $\pm 2k_{\rm SO}$. Their spin orientation is locked to the propagation direction and is determined by the sign of the RSOC α. The spin orientation is shown for the case $\alpha > 0$. The low energy massless and massive modes are highlighted with the same colors as in figure 4.

still has a minimum $E_+^{\rm min} = +E_{\rm Z}$ at $k = 0$, while the lower band has a local maximum at $k = 0$ and acquires two degenerate minima $E_-^{\rm min} = -E_{\rm SO} - E_{\rm Z}^2/4E_{\rm SO}$ at $k = \pm k_{\rm SO}\sqrt{1 - E_{\rm Z}^2/4E_{\rm SO}^2}$.

In the following we shall focus on the deep Rashba-dominated regime ($E_{\rm Z} \ll 2E_{\rm SO}$), illustrated in figure 4, and analyze the energy window inside the magnetic gap ($|E| \ll E_{\rm Z}$), highlighted by the dashed box. As is well known, in this range the NW propagating eigenstates are helical [17–19, 28–33]: their dispersion relation is well described by a linear behavior near the Fermi points $k \simeq \pm 2k_{\rm SO}$, while their spin orientation, mainly dictated by the Rashba term, is locked to the propagation direction. For $\alpha > 0$, right-moving electrons near the right Fermi point $k \simeq +2k_{\rm SO}$ are characterized by spin-↑, while left-moving electrons near the left Fermi point $k \simeq -2k_{\rm SO}$ have spin-↓ (see figure 4). The opposite occurs if $\alpha < 0$. The dynamics of these low energy propagating modes, which we shall denote by $\hat{\xi}_\uparrow$, $\hat{\xi}_\downarrow$, is thus described by a massless Dirac Hamiltonian. Note that the presence of one single Dirac cone is not an artifact of the continuum model (36) and can be found also in a regularized lattice version of it (see appendix C). Importantly, the helicity of the Dirac cone is determined by the *sign* of the RSOC α

$$s_\alpha = \mathrm{sgn}(\alpha). \tag{41}$$

This suggests that a junction between two NW regions with opposite values of RSOC realizes the Dirac paradox configuration.

However, as highlighted by the green lines in figure 4, the NW also exhibits low-energy gapped modes near $k = 0$, whose spin components shall be denoted as $\hat{\eta}_\uparrow$ and $\hat{\eta}_\downarrow$. Notably, these modes turn out to behave as massive Dirac fermions with a mass term $\Delta = E_{\rm Z}$. In problems involving homogeneous NWs these modes are dropped because they are not normalizable. However, as observed in section 3, in inhomogeneous problems such as the Dirac paradox configuration they describe evanescent waves that, despite carrying no current, ensure the wavefunction matching at the interface. For these reasons, the effective low energy theory capturing the physical properties of the Dirac paradox configuration realized with NWs is a Dirac model involving both massless and massive modes.

To derive such effective theory describing low energy excitations $|E| \ll E_{\rm Z} \ll 2E_{\rm SO}$, we assume that the ground state is the Fermi sea where all NW states below the midgap energy ($E < 0$) are occupied, and we perform an expansion near the points $k \simeq \pm 2k_{\rm SO}$ and $k \simeq 0$. It is possible to show (details can be found in appendix B), that the low energy excitations of the NW Hamiltonian are equivalent to low energy excitations of the massless + massive Dirac model

$$\begin{aligned}\hat{\mathcal{H}}_{\rm NW} = &\sum_{q=-\infty}^{+\infty} (\hat{\xi}_{q\uparrow}^\dagger \ \hat{\xi}_{q\downarrow}^\dagger) \begin{pmatrix} \hbar s_\alpha v_{\rm SO} q & 0 \\ 0 & -\hbar s_\alpha v_{\rm SO} q \end{pmatrix} \begin{pmatrix} \hat{\xi}_{q\uparrow} \\ \hat{\xi}_{q\downarrow} \end{pmatrix} \\ &+ \sum_{q=-\infty}^{+\infty} (\hat{\eta}_{q\uparrow}^\dagger \ \hat{\eta}_{q\downarrow}^\dagger) \begin{pmatrix} -\hbar s_\alpha v_{\rm SO} q & -E_{\rm Z} \\ -E_{\rm Z} & \hbar s_\alpha v_{\rm SO} q \end{pmatrix} \begin{pmatrix} \hat{\eta}_{q\uparrow} \\ \hat{\eta}_{q\downarrow} \end{pmatrix},\end{aligned} \tag{42}$$

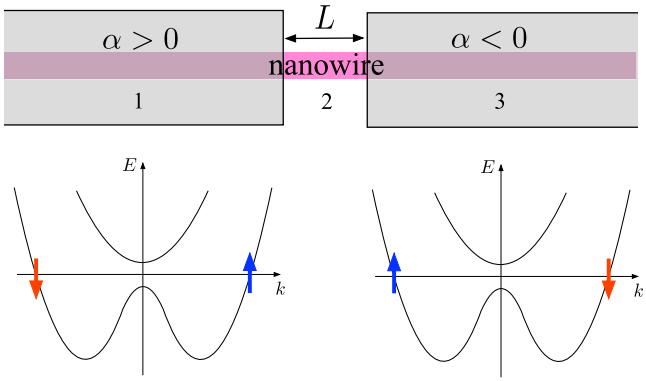


Figure 5. By gating different portions of the NW with metallic electrodes an inhomogeneous RSOC like (48) can be realized. Inside the Zeeman gap, induced by an external magnetic field applied along the NW axis, the helical states in the two outer regions have opposite helicity and thus realize the Dirac paradox configuration.

where $v_{\rm SO} = \hbar k_{\rm SO}/m^*$. Introducing the low-energy fields ($\sigma = \uparrow, \downarrow$)

$$\hat{\xi}_\sigma(x) = \frac{1}{\sqrt{\Omega}}\sum_q \hat{\xi}_{q,\sigma}\, \mathrm{e}^{\mathrm{i}qx} \qquad \hat{\eta}_\sigma(x) = \frac{1}{\sqrt{\Omega}}\sum_q \hat{\eta}_{q,\sigma}\, \mathrm{e}^{\mathrm{i}qx} \tag{43}$$

that physically describe excitations varying over lengthscales much longer than the spin–orbit length $l_{\rm SO} = k_{\rm SO}^{-1}$, the NW Hamiltonian can be expressed as

$$\hat{\mathcal{H}}_{\rm NW} = \int \mathrm{d}x\, \hat{\Psi}^\dagger(x) \left(s_\alpha v_{\rm SO} \tau_z \sigma_z p_x - \frac{E_{\rm Z}}{2}(\tau_0 - \tau_z)\sigma_x \right) \hat{\Psi}(x) \tag{44}$$

where $\hat{\Psi}(x) = (\hat{\xi}_\uparrow, \hat{\xi}_\downarrow, \hat{\eta}_\uparrow, \hat{\eta}_\downarrow)^{\rm T}$ is a four-component spinor field. One can now realize the connection between the NW Hamiltonian (44) and the model introduced in section 3 in equation (19). Indeed, identifying $v_{\rm SO} \to v_{\rm F}$ and $E_{\rm Z} \to \Delta$, equation (44) describes one side of the junction model (19), where the sign s_α of the RSOC (see equation (41)) implements the condition equation (20) or (21) and determines which side of the junction is described.

Finally, the original field $\hat{\Phi}$ can be expressed in terms of the Dirac slowly varying modes $(\hat{\xi}, \hat{\eta})$ and the fast oscillating plane waves related to the midgap Dirac points, as follows

$$\begin{pmatrix} \hat{\Phi}_\uparrow(x) \\ \hat{\Phi}_\downarrow(x) \end{pmatrix} = \begin{pmatrix} \mathrm{e}^{+2\mathrm{i}s_\alpha k_{\rm SO} x}\, \hat{\xi}_\uparrow(x) + \hat{\eta}_\uparrow(x) \\ \mathrm{e}^{-2\mathrm{i}s_\alpha k_{\rm SO} x}\, \hat{\xi}_\downarrow(x) + \hat{\eta}_\downarrow(x) \end{pmatrix}. \tag{45}$$

4.2. The case of inhomogeneous RSOC

Because the helicity of the NW low energy massless modes is determined by the sign of the RSOC, one can envisage a setup where two different NW portions are characterized by values of α with opposite signs, as illustrated in figure 5. Indeed the huge advances of gating techniques enable one to realize different gate potentials to various portions of the NWs [38–43], thereby locally varying the magnitude and even the sign of the RSOC [44–57]. The overall system can thus be described by a *inhomogeneous* spin–orbit coupling $\alpha(x)$ and the Hamiltonian (36) is generalized to [63–71]

$$H(x) = \frac{p_x^2}{2m^*}\sigma_0 - \frac{\{\alpha(x), p_x\}}{2\hbar}\sigma_z - h_x\sigma_x, \tag{46}$$

where the anticommutator is necessary since p_x does not commute with the space-dependent RSOC. In particular, as an elementary building block, one can consider a step-like RSOC profile $\alpha(x) = \alpha_{\rm L} H(x_0 - x) + \alpha_{\rm R} \mathrm{H}(x - x_0)$ describing an interface located at x_0 between two regions with RSOC equal to $\alpha_{\rm L}$ and $\alpha_{\rm R}$. In such a configuration one can straightforwardly derive the following

matching conditions [70]

$$\begin{cases} \hat{\Phi}_\uparrow(x_0^-) = \hat{\Phi}_\uparrow(x_0^+) \\ \hat{\Phi}_\downarrow(x_0^-) = \hat{\Phi}_\downarrow(x_0^+) \\ \partial_x\hat{\Phi}_\uparrow(x_0^-) = \partial_x\hat{\Phi}_\uparrow(x_0^+) - \mathrm{i}\dfrac{m^*}{\hbar^2}(\alpha_\mathrm{R} - \alpha_\mathrm{L})\hat{\Phi}_\uparrow(x_0) \\ \partial_x\hat{\Phi}_\downarrow(x_0^-) = \partial_x\hat{\Phi}_\downarrow(x_0^+) + \mathrm{i}\dfrac{m^*}{\hbar^2}(\alpha_\mathrm{R} - \alpha_\mathrm{L})\hat{\Phi}_\downarrow(x_0). \end{cases} \tag{47}$$

This provides all the ingredients for a concrete implementation of the Dirac paradox. In order to be more realistic, we shall consider a three-region configuration where the RSOC varies as

$$\alpha(x) = \begin{cases} +\alpha > 0 & \text{for } x < -L/2 \ \ (\text{region } 1) \\ 0 & \text{for } |x| < L/2 \ \ (\text{region } 2)\,, \\ -\alpha < 0 & \text{for } x > +L/2 \ \ (\text{region } 3) \end{cases} \tag{48}$$

where the two outer regions 1 and 3 with opposite RSOC are both assumed in the deep Rashba-dominated regime ($2E_\mathrm{SO} \gg E_\mathrm{Z}$), and are separated by the central crossover region 2 with length L and with vanishing RSOC, i.e. in the Zeeman-dominated regime (see figure 5).

Applying the general interface condition (47) to the two interfaces $x_1 = -L/2$ and $x_2 = +L/2$ of the piecewise constant profile (48), one can match the NW wavefunction in the three regions and obtain the solution for the NW scattering problem with standard techniques [72] (see appendix D). Although the resulting transmission coefficient is numerically exact and available for arbitrary values of E, E_SO and E_Z, it is not quite amenable. However, in the energy window $|E| \ll E_\mathrm{Z} \ll 2E_\mathrm{SO}$ where the Dirac paradox emerges, an analytical expression can be gained from the effective low energy model. To this purpose, one can insert the expression (45) for the field $\hat{\Phi}$ in the outer Rashba-dominated regions into the interface condition (47) and obtain the low energy boundary conditions at the left interface $x_1 = -L/2$

$$\begin{cases} \mathrm{e}^{-\mathrm{i}k_\mathrm{SO}L}\hat{\xi}_\uparrow(x_1^-) + \hat{\eta}_\uparrow(x_1^-) = \hat{\Phi}_\uparrow(x_1^+) \\ \mathrm{e}^{+\mathrm{i}k_\mathrm{SO}L}\hat{\xi}_\downarrow(x_1^-) + \hat{\eta}_\downarrow(x_1^-) = \hat{\Phi}_\downarrow(x_1^+) \\ +\mathrm{i}k_\mathrm{SO}\left[\mathrm{e}^{-\mathrm{i}k_\mathrm{SO}L}\,\hat{\xi}_\uparrow(x_1^-) - \hat{\eta}_\uparrow(x_1^-)\right] = \partial_x\hat{\Phi}_\uparrow(x_1^+) \\ -\mathrm{i}k_\mathrm{SO}\left[\mathrm{e}^{+\mathrm{i}k_\mathrm{SO}L}\,\hat{\xi}_\downarrow(x_1^-) - \hat{\eta}_\downarrow(x_1^-)\right] = \partial_x\hat{\Phi}_\downarrow(x_1^+) \end{cases} \tag{49}$$

and at the right interface $x_2 = +L/2$

$$\begin{cases} \hat{\Phi}_\uparrow(x_2^-) = \mathrm{e}^{-\mathrm{i}k_\mathrm{SO}L}\hat{\xi}_\uparrow(x_2^+) + \hat{\eta}_\uparrow(x_2^+) \\ \hat{\Phi}_\downarrow(x_2^-) = \mathrm{e}^{+\mathrm{i}k_\mathrm{SO}L}\hat{\xi}_\downarrow(x_2^+) + \hat{\eta}_\downarrow(x_2^+) \\ \partial_x\hat{\Phi}_\uparrow(x_2^-) = -\mathrm{i}k_\mathrm{SO}\left[\mathrm{e}^{-\mathrm{i}k_\mathrm{SO}L}\hat{\xi}_\uparrow(x_2^+) - \hat{\eta}_\uparrow(x_2^+)\right] \\ \partial_x\hat{\Phi}_\downarrow(x_2^-) = +\mathrm{i}k_\mathrm{SO}\left[\mathrm{e}^{+\mathrm{i}k_\mathrm{SO}L}\hat{\xi}_\downarrow(x_2^+) - \hat{\eta}_\downarrow(x_2^+)\right] \end{cases}, \tag{50}$$

where, consistently with the low energy limit, we have neglected the derivatives $\partial_x\hat{\xi}$ and $\partial_x\hat{\eta}$ of the slowly varying fields with respect to the term proportional to k_SO, since they are characterized by wavevectors $|q| \ll k_\mathrm{SO}$.

In the central region 2, where only the Zeeman coupling is present, the field $\hat{\Phi}$ can be expressed as a linear combination of propagating and evanescent waves that are eigenfunctions of σ_x, so that for $|x| < L/2$

$$\hat{\Phi}(x) = \frac{\hat{h}_E}{\sqrt{2}}\begin{pmatrix}1\\1\end{pmatrix}\mathrm{e}^{\mathrm{i}k_{2,E}x} + \frac{\hat{g}_E}{\sqrt{2}}\begin{pmatrix}1\\1\end{pmatrix}\mathrm{e}^{-\mathrm{i}k_{2,E}x} + \frac{\hat{d}_E}{\sqrt{2}}\begin{pmatrix}1\\-1\end{pmatrix}\mathrm{e}^{\kappa_{2,E}x} + \frac{\hat{f}_E}{\sqrt{2}}\begin{pmatrix}1\\-1\end{pmatrix}\mathrm{e}^{-\kappa_{2,E}x}, \tag{51}$$

where $\hat{h}_E, \hat{g}_E, \hat{d}_E$ and $\hat{f}_E$ are mode operators, whereas $k_{2,E} = k_\mathrm{Z}\sqrt{1 + E/E_\mathrm{Z}}$, $\kappa_{2,E} = k_\mathrm{Z}\sqrt{1 - E/E_\mathrm{Z}}$ and k_Z is given in equation (40). Inserting equation (51) into equations (49) and (50), one can obtain the link

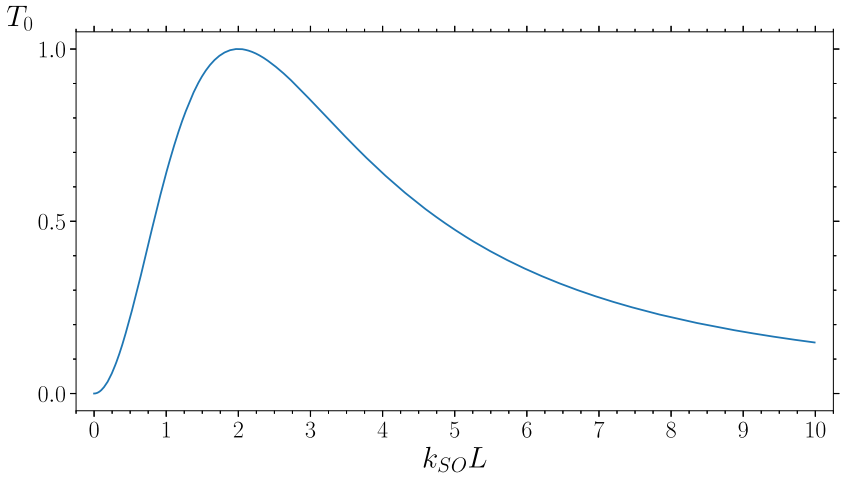


Figure 6. The transmission coefficient (57), plotted as a function of $k_{\mathrm{SO}}L$, covers the entire range $T_0 \in [0, 1]$.

between the fields in the outer Rashba-dominated regions

$$\begin{pmatrix} \hat{\xi}_\uparrow(L/2) \\ \hat{\xi}_\downarrow(L/2) \\ \hat{\eta}_\uparrow(L/2) \\ \hat{\eta}_\downarrow(L/2) \end{pmatrix} = \mathsf{M}_E \begin{pmatrix} \hat{\xi}_\uparrow(-L/2) \\ \hat{\xi}_\downarrow(-L/2) \\ \hat{\eta}_\uparrow(-L/2) \\ \hat{\eta}_\downarrow(-L/2) \end{pmatrix}, \tag{52}$$

where the transfer matrix M_E depends on the energy E and on the size L of the central region through two dimensionless parameters $k_{\mathrm{Z}}L$ and $k_{\mathrm{SO}}L$. Details about the derivation of M_E can be found in the appendix D. As an illustrative example, here we shall focus on the midgap value ($E = 0$), which in fact well represents the entire low energy range $|E| \ll E_{\mathrm{Z}}$. Moreover, since in the deep Rashba-dominated regime $k_{\mathrm{Z}}L \ll k_{\mathrm{SO}}L$, one can keep $k_{\mathrm{SO}}L$ finite and consider $k_{\mathrm{Z}}L$ as a small parameter, performing an expansion of $\mathsf{M}_{E=0}$ in its powers. Neglecting orders $O((k_{\mathrm{Z}}L)^4)$ one obtains

$$\mathsf{M}_0 \simeq \begin{pmatrix} \mathrm{i}k_{\mathrm{SO}}L/2 & A & (1 - \mathrm{i}k_{\mathrm{SO}}L/2)\mathrm{e}^{\mathrm{i}k_{\mathrm{SO}}L} & B \\ A^* & -\mathrm{i}k_{\mathrm{SO}}L/2 & B^* & (1 + \mathrm{i}k_{\mathrm{SO}}L/2)\mathrm{e}^{-\mathrm{i}k_{\mathrm{SO}}L} \\ (1 + \mathrm{i}k_{\mathrm{SO}}L/2)\mathrm{e}^{-\mathrm{i}k_{\mathrm{SO}}L} & -B & -\mathrm{i}k_{\mathrm{SO}}L/2 & A^*\,\mathrm{e}^{2\mathrm{i}Lk_{\mathrm{SO}}} \\ -B^* & (1 - \mathrm{i}k_{\mathrm{SO}}L/2)\mathrm{e}^{\mathrm{i}k_{\mathrm{SO}}L} & A\,\mathrm{e}^{-2\mathrm{i}k_{\mathrm{SO}}L} & \mathrm{i}k_{\mathrm{SO}}L/2 \end{pmatrix}, \tag{53}$$

where

$$A = \mathrm{i}\frac{-6 + k_{\mathrm{SO}}L(k_{\mathrm{SO}}L + 6i)}{12k_{\mathrm{SO}}L}\,\mathrm{e}^{2\mathrm{i}Lk_{\mathrm{SO}}}(k_{\mathrm{Z}}L)^2 \tag{54}$$

$$B = -\mathrm{i}\frac{(k_{\mathrm{SO}}L)^2 + 6}{12k_{\mathrm{SO}}L}\mathrm{e}^{\mathrm{i}k_{\mathrm{SO}}L}(k_{\mathrm{Z}}L)^2. \tag{55}$$

The eight entries of the transfer matrix (53) containing A and B couple spin-↑ to spin-↓ components. Notably, such terms are of the order $O((k_{\mathrm{Z}}L)^2)$ and in the regime $k_{\mathrm{Z}}L \ll 1$ can be neglected with respect to the other terms, which are $O(1)$ with respect to the variable $k_{\mathrm{Z}}L$. Then, the transfer matrix reduces to

$$\mathsf{M}_0 \simeq \begin{pmatrix} \mathrm{i}\frac{k_{\mathrm{SO}}L}{2} & 0 & \left(1 - \mathrm{i}\frac{k_{\mathrm{SO}}L}{2}\right)\mathrm{e}^{\mathrm{i}k_{\mathrm{SO}}L} & 0 \\ 0 & -\mathrm{i}\frac{k_{\mathrm{SO}}L}{2} & 0 & \left(1 + \mathrm{i}\frac{k_{\mathrm{SO}}L}{2}\right)\mathrm{e}^{-\mathrm{i}k_{\mathrm{SO}}L} \\ \left(1 + \mathrm{i}\frac{k_{\mathrm{SO}}L}{2}\right)\mathrm{e}^{-\mathrm{i}k_{\mathrm{SO}}L} & 0 & -\mathrm{i}\frac{k_{\mathrm{SO}}L}{2} & 0 \\ 0 & \left(1 - \mathrm{i}\frac{k_{\mathrm{SO}}L}{2}\right)\mathrm{e}^{\mathrm{i}k_{\mathrm{SO}}L} & 0 & \mathrm{i}\frac{k_{\mathrm{SO}}L}{2} \end{pmatrix}. \tag{56}$$

The expression (56) has precisely the form equation (28) of the transfer matrix of the massless + massive Dirac model described in section 3, when setting $\beta_\uparrow = -\beta_\downarrow = k_{\mathrm{SO}}L/2$, $\chi_\uparrow = -\chi_\downarrow = k_{\mathrm{SO}}L$ and

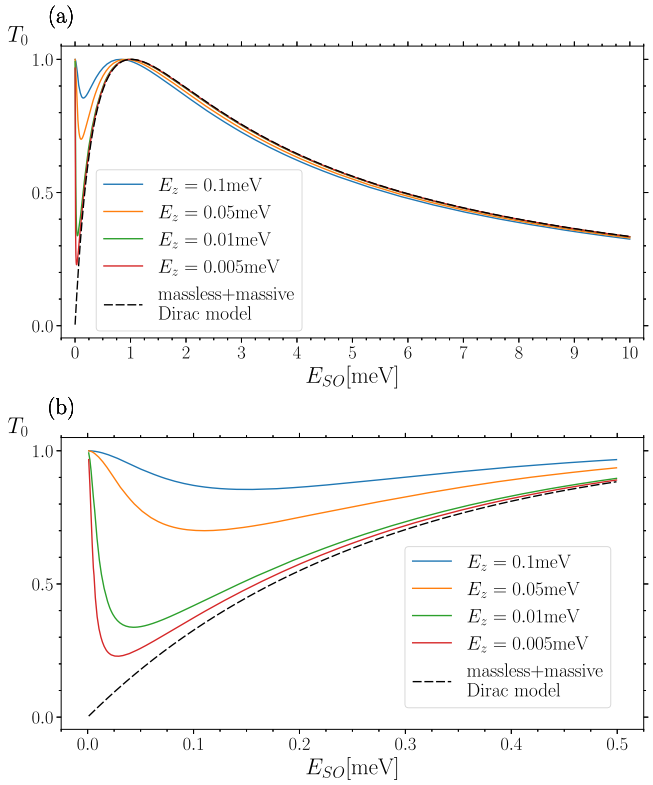


Figure 7. The Dirac paradox configuration realized with a InSb NW setup where two outer gated regions are characterized by opposite RSOC and the central region has a width $L = 100$ nm (see figure 5). The midgap transmission coefficient ($E = 0$), obtained from the numerically exact solution of the model (46) with the profile (48), is plotted as a function of the spin orbit energy, for different values of the external magnetic field E_Z (solid curves). When the Rashba-dominated regime ($2E_{SO} \gg E_Z$) is reached, the various solid curves all tend to the dashed curve describing the result equation (57), obtained in the low energy limit from the effective massless + massive Dirac model. Panel (b) is a zoom of panel (a) in the regime of spin–orbit values that are realistic with present gating techniques.

$\gamma_\uparrow = \gamma_\downarrow = \nu_\uparrow = \nu_\downarrow = 0$. Thus, in the regime $k_Z L \ll 1$, where the central region is much shorter than the Zeeman wavelength $l_Z = k_Z^{-1}$ characterizing the wavefunction (51) at $E = 0$, the transfer matrix is diagonal in spin and becomes independent of the Zeeman energy E_Z. Yet, M_0 couples massless to massive modes and still depends on $k_{SO}L$. This parameter, which represents the ratio of the crossover region L to the spin–orbit length $l_{SO} = k_{SO}^{-1}$, may be finite because of the deep Rashba-dominated regime $k_Z \ll k_{SO}$.

In turn, the transmission coefficient related to equation (56) can be obtained from the general formula equation (34),

$$T_0 = \frac{(k_{SO}L)^2}{\left(1 + (k_{SO}L/2)^2\right)^2}, \tag{57}$$

and varies over the entire range $T_0 \in [0, 1]$ as a function of $k_{SO}L$, as shown in figure 6. In particular, while for small values $k_{SO}L \ll 1$ the transmission is low, $T_0 \sim (k_{SO}L)^2$, for finite values of $k_{SO}L$ we observe from figure 6 that T_0 increases, and a perfect transmission $T_0 = 1$ is obtained for $k_{SO}L = 2$. Then, for large values of $k_{SO}L$ the transmission decreases again as $T_0 \sim 16/(k_{SO}L)^2$. The ratio of the spin–orbit length $l_{SO} = k_{SO}^{-1}$ to the distance L is thus the parameter controlling the value of T_0.

4.3. Transmission coefficient in the case of InSb

For definiteness, we consider here an implementation with a ballistic InSb NW with effective electron mass $m^* = 0.015m_e$. Two different portions of the NW are supposed to be gated by differently biased metals inducing opposite RSOC values, as previously sketched in figure 5, and are separated by a crossover region $L = 100$ nm where the RSOC is negligible. In figure 7(a) the solid curves display the midgap transmission coefficient $T_0 = T_{E=0}$ as a function of the spin–orbit energy E_{SO}, for different values of the Zeeman energy E_Z, obtained from the numerically exact solution of the model (46) with the profile (48) (see appendix D for technical details). Moreover the dashed curve describes the analytical result (57) obtained from the low-energy limit in the Rashba-dominated regime of the outer regions, i.e. the massless + massive Dirac model. As one can see, for $E_{SO} \to 0$, the exact transmission coefficient tends to 1, regardless of the value of E_Z, since all three regions become equal in such a limit. However, for each Zeeman energy value, when E_{SO} is sufficiently large to enter the deep Rashba-dominated regime ($2E_{SO} \gg E_Z$), all solid curves are well

reproduced by the low-energy limit equation (57) (dashed curve), which is independent of E_Z. This is thus the regime where the NW gap states are helical and the setup realizes the Dirac paradox. Despite the absence of a spin-active interface, the transmission coefficient is non-vanishing because the propagating massless modes are coupled to the evanescent massive modes. In figure 7(b) the same quantities as in panel (a) are shown, with a zoom in the range of spin–orbit energy values up to $E_{SO} = 0.5$ meV, which is the realistic range presently reachable. Correspondingly, the range of Zeeman energy values E_Z ensuring a deep Rashba dominated regime for the external gated regions is $E_Z < 0.1$ meV. This implies that the linear conductance G_0, straightforwardly connected to the transmission coefficient through the relation $G_0 = (e^2/h)T_{E=0}$, is tunable from low to high values with varying the spin–orbit energy, which can electrically be done through the gate voltage.

Note that the electric field due to the gate is perpendicular to the NW axis, and the current flowing along the NW is the response to the difference in the electrochemical potentials of the two reservoirs connected to the NW. In the quantum ballistic regime considered here, the case of an electric field longitudinal to the NW axis could be realized by exposing the NW to an external electrical radiation field. Although such analysis goes far beyond the scope of the present paper, we mention here that, as far as the NW helical states are concerned, such problem is similar to the one studied for the helical states in quantum spin Hall systems. In that case, a photocurrent can be generated by a suitably localized electric pulse, and signatures of chiral anomaly due to the helical states can be found in the chemical and temperature dependence of the spin-polarized photo-excited wavepackets [73]. A similar scenario can thus be expected for NWs as well.

5. Conclusions

In this paper we have analyzed the Dirac paradox, illustrated in figure 1, where an electron impinging towards an interface can seemingly neither be transmitted nor reflected. In particular, we have focussed on the interesting case of one spatial dimension. Indeed, differently from higher dimensional realizations such as heterojunctions between two 3D topological insulators where electrons can leak along the interface surface, in 1D electrons do not have a 'way out' to escape the paradox. We have first analyzed models that purely involve massless modes. The first model equation (2), where the helicity change across the interface is accounted for by a spatially inhomogeneous velocity, leads to conclude that the paradox has no actual solution, namely it is not possible to build up a scattering state solution. Indeed physical solutions must necessarily involve electron injection from both sides and are characterized by a vanishing current. In contrast, the second model equation (13), where the helicity change occurs through a rotation of the spin across the interface, provides a trivial solution to the paradox, for it directly introduces a spin-active interface, which leads to a perfect transmission.

Then, we have proposed a model, equation (19), involving both massless and massive Dirac modes (see figure 2) and we have shown that it leads to a non-trivial solution of the Dirac paradox, even for a spin-inactive interface. This is possible because of the massive modes that, despite carrying no current for energies inside their gap, always exhibit both spin components. Thus, a massless–massive coupling at the interface indirectly enable an incoming massless electron impinging with spin-↑ to get transmitted as a massless electron with spin-↓ (see figure 3). Properly defined scattering state solutions thus exist, and the transmission coefficient depends in general on three parameters (see equation (34)).

Moreover, in section 4, we have shown that such model can be implemented in spin–orbit coupled NWs exposed to an external magnetic field, whose midgap states are characterized by massless modes near the Fermi points $k \sim \pm 2k_{SO}$ and massive modes near $k \sim 0$ (see figure 4). The massless modes are helical in the deep Rashba-dominated regime ($2E_{SO} \gg E_Z$) and their helicity is determined by the sign of the RSOC. Because the latter can be tuned by state-of-the-art gating techniques, a NW with two regions characterized by opposite RSOC values, as shown in figure 5, is a suitable candidate to realize the Dirac paradox configuration in one spatial dimension. We have shown that the low energy limit of such inhomogeneous NW model is precisely a particular case of the proposed model (19). The resulting transmission coefficient (57) varies over the full range $T_0 \in [0, 1]$ (see figure 6) as a function of the parameter $k_{SO}L$, where L is the distance between the two differently gated regions and k_{SO} is the spin–orbit wavevector that is directly controlled by the RSOC (see equation (39)). Focussing on the specific case of an inhomogeneous InSb NW, we have determined from model (46) the exact transmission coefficient, which in general depends both on the spin–orbit and the Zeeman energies (solid curves of figure 7). Whenever the Rashba-dominated regime is reached, the setup realizes the Dirac paradox configuration. Then, the transmission coefficient is well captured by the low energy limit result (57) (dashed curve of figure 7) obtained from the proposed massless + massive Dirac model and only depends on the spin–orbit energy E_{SO}. Because E_{SO} can be controlled via the gate bias coupled to the NW, the transmission coefficient and the

linear conductance are electrically tuneable. These results thus represent a conceptual advance in the understanding of Dirac heterojunctions and pave the way to fruitful applications of the helical states realized in spin–orbit coupled NWs.

Acknowledgments

Discussions with Björn Trauzettel, Christoph Fleckenstein and Niccolò Traverso Ziani in the early stage of this work are acknowledged.

Data availability statement

The data that support the findings of this study are available upon reasonable request from the authors.

Appendix A. Derivation of the transfer matrix equation (28)

In this appendix we provide details about the derivation of the transfer matrix (28), i.e. the most general 4×4 matrix fulfilling the requirements (26) and (27). We first observe that the former requirement (26) straightforwardly stems from equation (21) and the property $(U_{\mathrm{R}}^{\dagger})^{-1} = (U_{\mathrm{R}}^{-1})^{\dagger}$, which imply that U_{R}^{-1} fulfills equation (21) as well. When taking into account equation (20) and the definition (25), the condition (26) follows. Second, we observe that the requirement (27) can equivalently be formulated by requiring that M must only involve the combinations $\sigma_{\uparrow} = (\sigma_0 + \sigma_z)/2$ and $\sigma_{\downarrow} = (\sigma_0 - \sigma_z)/2$, i.e. M must have the form

$$\mathsf{M} = \mathsf{M}_{\uparrow}\sigma_{\uparrow} + \mathsf{M}_{\downarrow}\sigma_{\downarrow}, \tag{A1}$$

where $\mathsf{M}_{\uparrow,\downarrow}$ are 2×2 matrices acting on the massless–massive pseudospin space and fulfilling

$$\mathsf{M}_{\sigma}^{\dagger}\tau_z\mathsf{M}_{\sigma} = -\tau_z \quad \sigma = \uparrow,\downarrow \tag{A2}$$

as a consequence of equation (26) and of the properties $\sigma_{\uparrow,\downarrow}^2 = \sigma_{\uparrow,\downarrow}$ and $\sigma_{\uparrow}\sigma_{\downarrow} = [\sigma_{\uparrow}, \sigma_z] = [\sigma_{\downarrow}, \sigma_z] = 0$. For each spin sector $\sigma = \uparrow,\downarrow$, the requirement equation (A2) imposed on a generic 2×2 complex matrix

$$\mathsf{M}_{\sigma} = \begin{pmatrix} a_{\sigma} & b_{\sigma} \\ c_{\sigma} & d_{\sigma} \end{pmatrix} \tag{A3}$$

implies that $|c_{\sigma}|^2 - |a_{\sigma}|^2 = 1$, $|b_{\sigma}|^2 - |d_{\sigma}|^2 = 1$ and $a_{\sigma}^{*}b_{\sigma} = c_{\sigma}^{*}d_{\sigma}$. These conditions straightforwardly imply the following expression

$$\mathsf{M}_{\sigma} = \mathrm{e}^{\mathrm{i}\nu_{\sigma}} \begin{pmatrix} \mathrm{i}\beta_{\sigma}\,\mathrm{e}^{-\mathrm{i}\gamma_{\sigma}} & (1 - \mathrm{i}\beta_{\sigma})\,\mathrm{e}^{\mathrm{i}\chi_{\sigma}} \\ (1 + \mathrm{i}\beta_{\sigma})\,\mathrm{e}^{-\mathrm{i}\chi_{\sigma}} & -\mathrm{i}\beta_{\sigma}\,\mathrm{e}^{\mathrm{i}\gamma_{\sigma}} \end{pmatrix}, \tag{A4}$$

which also fulfills the properties $\mathsf{M}_{\sigma}^{-1}(\beta_{\sigma}, \chi_{\sigma}, \nu_{\sigma}, \gamma_{\sigma}) = \mathsf{M}_{\sigma}(\beta_{\sigma}, \chi_{\sigma}, -\nu_{\sigma}, -\gamma_{\sigma})$ and $\det(\mathsf{M}_{\sigma}) = -\exp[2\mathrm{i}\nu_{\sigma}]$. Inserting the two independent matrices $\mathsf{M}_{\uparrow}$ and $\mathsf{M}_{\downarrow}$ given in equation (A4) into equation (A1), the transfer matrix M in the $\tau \otimes \sigma$ basis takes the form given in equation (28).

Finally, an explicit expression can be given for U_{L} and U_{R} as well. The requirement (20) can always be fulfilled by choosing for U_{L} the form

$$U_{\mathrm{L}} = \tau_0\sigma_0. \tag{A5}$$

Then, the expression for $U_{\mathrm{R}} = \mathsf{M}^{-1}$ following from equation (25) can straightforwardly be obtained from equation (28) by exploiting the property $\mathsf{M}^{-1}(\boldsymbol{\beta}, \boldsymbol{\chi}, \boldsymbol{\nu}, \boldsymbol{\gamma}) = \mathsf{M}(\boldsymbol{\beta}, \boldsymbol{\chi}, -\boldsymbol{\nu}, -\boldsymbol{\gamma})$, where each bold symbols denotes the pair of related parameters, e.g. $\boldsymbol{\beta} = (\beta_{\uparrow}, \beta_{\downarrow})$.

Appendix B. Details about the NW Hamiltonian and its low energy limit

For the sake of completeness, we provide here some details about the NW Hamiltonian described in section 4.1. Denoting by Ω the total NW length and re-expressing the field in terms of its Fourier modes $\hat{C}_k = (\hat{c}_{k\uparrow},\ \hat{c}_{k\downarrow})^{\mathrm{T}}$

$$\begin{pmatrix} \hat{\Phi}_{\uparrow}(x) \\ \hat{\Phi}_{\downarrow}(x) \end{pmatrix} = \frac{1}{\sqrt{\Omega}} \sum_{k} \mathrm{e}^{\mathrm{i}kx} \begin{pmatrix} \hat{c}_{k\uparrow} \\ \hat{c}_{k\downarrow} \end{pmatrix}, \tag{B1}$$

the NW Hamiltonian $\hat{\mathcal{H}}_{\mathrm{NW}}$ is compactly rewritten in terms of a 2×2 matrix $H_{\mathrm{NW}}(k)$, i.e. $\hat{\mathcal{H}}_{\mathrm{NW}} = \sum_k \hat{C}_k^{\dagger} H_{\mathrm{NW}}(k) \hat{C}_k$. In turn, this also highlights the energy scales involved in the problem. In

particular, the first two terms acquire the form

$$\hat{\mathcal{H}}_{\rm kin}+\hat{\mathcal{H}}_{\rm R}=\sum_k \hat{C}_k^\dagger\left(\frac{\hbar^2}{2m^*}(k\sigma_0-s_\alpha k_{\rm SO}\sigma_z)^2-E_{\rm SO}\sigma_0\right)\hat{C}_k \tag{B2}$$

and describe two parabolic spin bands that are lowered by the spin–orbit energy (37) and horizontally shifted by the spin–orbit wavevector (39) with the sign (41) of the RSOC determining whether the shift is positive or negative in k-axis. Assuming $h_x>0$ for definiteness, the Zeeman term is rewritten as

$$H_{\rm Z}=-E_{\rm Z}\sum_k \hat{C}_k^\dagger\sigma_x\hat{C}_k, \tag{B3}$$

where $E_{\rm Z}$ is the Zeeman energy given in equation (38). Summing up equations (B2) and (B3) the diagonalization of the resulting $H_{\rm NW}(k)$ is straightforward. Denoting $\varepsilon_k^0=\hbar^2k^2/2m^*$, the spectrum consists of two energy bands

$$E_\pm(k)=\varepsilon_k^0\pm\sqrt{E_{\rm Z}^2+\alpha^2k^2}, \tag{B4}$$

separated at $k=0$ by a gap $2E_{\rm Z}$ centered around the midgap energy $E=0$. The eigenfunctions related to the spectrum (B4) are $\psi_{k,\pm}(x)=w_{k,\pm}\,\exp[ikx]/\sqrt{\Omega}$. They describe plane waves with spinors

$$w_{k,-}=\begin{pmatrix}\cos\dfrac{\theta_k}{2}\\ \sin\dfrac{\theta_k}{2}\end{pmatrix}\qquad w_{k,+}=\begin{pmatrix}-\sin\dfrac{\theta_k}{2}\\ \cos\dfrac{\theta_k}{2}\end{pmatrix}, \tag{B5}$$

whose spin orientation $\mathbf{n}(k)\equiv(\sin\,\theta_k,0,\cos\,\theta_k)$ lies on the xz-plane and depends on the wavevector k, forming with the z-axis an angle $\theta_k\in[0,\pi]$ defined through

$$\begin{cases}\cos\,\theta_k=\dfrac{\alpha k}{\sqrt{E_{\rm Z}^2+\alpha^2k^2}}\\ \sin\,\theta_k=\dfrac{E_{\rm Z}}{\sqrt{E_{\rm Z}^2+\alpha^2k^2}}\end{cases}. \tag{B6}$$

Furthermore, for energies $|E|<E_{\rm Z}$, the model also exhibits evanescent wave solutions $\tilde{\psi}_{\kappa,\pm}(x)=\tilde{w}_{\kappa,\pm}\,\exp[\kappa x]/\sqrt{\Omega}$. They describe plane waves with spinors

$$\tilde{w}_{\kappa,\pm}=\frac{1}{\sqrt{2}}\begin{pmatrix}\mp\exp\left[\pm{\rm i}\,\arctan\left(\alpha\kappa/\sqrt{E_{\rm Z}^2-(\alpha\kappa)^2}\right)\right]\\ 1\end{pmatrix} \tag{B7}$$

with energy $E_\pm=-\varepsilon_\kappa^0\pm\sqrt{E_{\rm Z}^2-(\alpha\kappa)^2}$. While these solutions are not normalizable in a homogeneous NW, they must be taken into account in the inhomogeneous RSOC problem.

Let us now focus on the regime ($|E|\ll E_{\rm Z}\ll 2E_{\rm SO}$) and derive an effective low energy NW Hamiltonian.

Expansion near $k=\pm2k_{\rm SO}$. In the deep Rashba-dominated regime ($E_{\rm Z}\ll 2E_{\rm SO}$), one finds that, up to $O\left((E_{\rm Z}/2E_{\rm SO})^2\right)$,

$$E_-(k)\approx 0\;\Leftrightarrow\;k\approx\pm2k_{\rm SO} \tag{B8}$$

$$\cos\,\theta_{k=\pm2k_{\rm SO}}\approx\pm s_\alpha, \tag{B9}$$

so that the spinors (B5) of the lower band propagating modes near $k\sim\pm2k_{\rm SO}$ reduce to eigenstates of σ_z, $(1,0)^{\rm T}$ or $(0,1)^{\rm T}$, depending on the sign s_α of the RSOC (see equation (41)). To extract the low energy Hamiltonian governing their dynamics, let us consider, for instance, $\alpha>0$ like in figure 4, and focus e.g. on the vicinity of the right Fermi point $+2k_{\rm SO}$. Setting $k=2k_{\rm SO}+q$ and performing an expansion of equations (B2) and (B3) for $|q|\ll k_{\rm SO}$, one obtains

$$\begin{aligned}\hat{\mathcal{H}}_{\rm NW}\Big|_{k\simeq+2k_{\rm SO}}&\simeq\sum_{|q|\ll k_{\rm SO}}\hat{C}_{2k_{\rm SO}+q}^\dagger\begin{pmatrix}\hbar v_{\rm SO}q & -E_{\rm Z}\\ -E_{\rm Z} & 8E_{\rm SO}\end{pmatrix}\hat{C}_{2k_{\rm SO}+q}\\ &\simeq\sum_{|q|\ll k_{\rm SO}}\hbar v_{\rm SO}q\,\hat{c}_{2k_{\rm SO}+q,\uparrow}^\dagger\hat{c}_{2k_{\rm SO}+q,\uparrow},\end{aligned} \tag{B10}$$

where $v_{\rm SO}=\hbar k_{\rm SO}/m^*$. The last line of equation (B10) follows from the fact that, while the spin-↑ band is characterized by a low-energy $\hbar v_{\rm F}q$, the spin-↓ band has a large energy $8E_{\rm SO}$ much above the magnetic gap.

The weak Zeeman energy $E_Z \ll 2E_{SO}$ cannot couple them, so that in the low energy sector $|E| \ll E_Z$ only the spin-↑ states matter. One can proceed in a similar manner near the $-2k_{SO}$ Fermi point, obtaining that only the spin-↓ states matter, proving that the states are helical. Repeating the same calculation for $\alpha < 0$ one obtains the opposite helicity. From equation (B10) the massless propagating low energy excitations ($|q| \ll k_{SO}$) are thus described by the set of operators

$$\begin{cases} \hat{\xi}_{q\uparrow} \doteq \hat{c}_{2s_\alpha k_{SO}+q,\uparrow} \\ \hat{\xi}_{q\downarrow} \doteq \hat{c}_{-2s_\alpha k_{SO}+q,\downarrow} \end{cases} \tag{B11}$$

where s_α is given by equation (41).

Expansion near $k = 0$. In the low energy range $|E| \ll E_Z$ there are also gapped (i.e. massive) modes, related to the upper and lower bands for $k \sim 0$ (see figure 4). Performing an expansion of equations (B2) and (B3) in $q = k$ (with $|q| \ll k_{SO}$) and introducing the new set of operators

$$\begin{cases} \hat{\eta}_{q\uparrow} = \hat{c}_{q\uparrow} \\ \hat{\eta}_{q\downarrow} = \hat{c}_{q\downarrow}, \end{cases} \tag{B12}$$

one obtains the low energy expression

$$\hat{\mathcal{H}}_{NW}\Big|_{k\simeq 0} \simeq -\sum_{|q|\ll k_{SO}} \hbar s_\alpha v_{SO} q \begin{pmatrix} \hat{\eta}^\dagger_{q\uparrow} & \hat{\eta}^\dagger_{q\downarrow} \end{pmatrix} \sigma_z \begin{pmatrix} \hat{\eta}_{q\uparrow} \\ \hat{\eta}_{q\downarrow} \end{pmatrix} - E_Z \sum_{|q|\ll k_{SO}} \begin{pmatrix} \hat{\eta}^\dagger_{q\uparrow} & \hat{\eta}^\dagger_{q\downarrow} \end{pmatrix} \sigma_x \begin{pmatrix} \hat{\eta}_{q\uparrow} \\ \hat{\eta}_{q\downarrow} \end{pmatrix}. \tag{B13}$$

Summing up equations (B10) and (B13) one obtains a low-energy NW Hamiltonian. Moreover, one can observe that such model shares the same low-energy physics as the Dirac model given in equation (42), obtained by removing the constraints on wave vector q, which can therefore be regarded to as the effective low energy model for the NW.

Appendix C. Lattice model

In this appendix we show that the existence of one single effective massless Dirac mode, i.e. a Weyl mode, inside the magnetic gap of the NW is not an artifact of the continuum model in equation (36). To this purpose, we consider the following lattice model

$$H = -t\sum_j \left(C^\dagger_{j+1} C_j + \mathrm{i}a C^\dagger_{j+1} \sigma_z C_j + b\, C^\dagger_j \sigma_x C_j - C^\dagger_j C_j \right) + \text{h.c.}, \tag{C1}$$

where $C^\dagger_j = (c^\dagger_{j\uparrow}, c^\dagger_{j\downarrow})$ and $c^\dagger_{j\uparrow,\downarrow}$ creates a fermion in the site j with spin ↑ or ↓, respectively. Here t is the nearest-neighbor hopping amplitude, while a and b are dimensionless parameters related to the strength of the spin–orbit coupling (time reversal preserving) and the external magnetic field (time reversal breaking), respectively. Passing to momentum space operators through $C_j = N^{-1/2}\sum_{k\in BZ} \mathrm{e}^{\mathrm{i}kja_0}\, C_k$, where N denotes the number of lattice sites, a_0 the lattice spacing and $ka_0 \in [-\pi, \pi]$ the lattice momentum, one gets

$$H = 2t\sum_k C^\dagger_k \left\{ [1 - \cos(ka_0)]\, \sigma_0 - a\, \sin(ka_0)\sigma_z - b\, \sigma_x \right\} C_k. \tag{C2}$$

It is straightforward to see that equation (C2) can be considered as the lattice regularized version of the continuum model in equation (36). Indeed in the limit $ka_0 \ll 1$, the former model reduces to the latter upon identifying $t = \hbar^2/2\, m^* a_0^2$, $a = m^* a_0 \alpha/\hbar^2$ and $b = h_x m^* a_0^2/\hbar^2$. The energy spectrum of the lattice model (C2) is easily obtained

$$E_\pm(k) = 2t \left[1 - \cos(k) \pm \sqrt{a^2 \sin^2(k) + b^2} \right], \tag{C3}$$

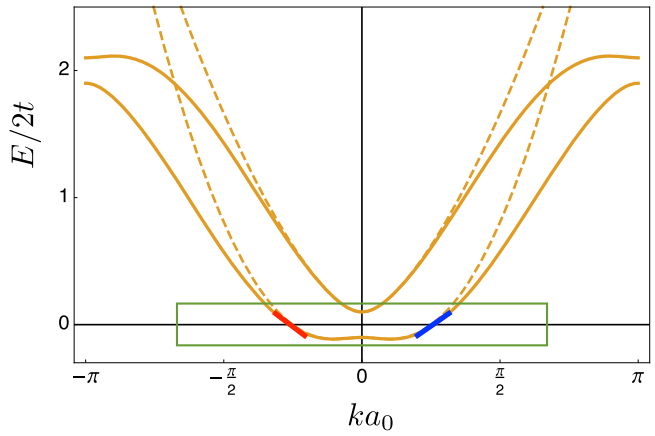


Figure 8. Comparison between the spectra of the lattice model equation (C2) (solid curves) and of the continuum model equation (36) (dashed curves). The latter captures the main features of the former in the low energy sector (green box). In particular only two helical states (red and blue thick lines) are present in the magnetic gap around $E = 0$.

and is plotted in figure 8 (solid lines), whereas the dashed lines display the spectrum of the continuum model (36) for comparison. As one can see, the low energy sector of the lattice model (green box) is perfectly captured by the continuum theory. In particular, the bands of the full lattice model cross the $E = 0$ line in *two and only two points*, namely the ones already found within the continuum model, since a gap is present at $k = 0$. Thus, inside the magnetic gap, one finds only two massless helical states (red and blue thick lines), i.e. *one* single 1D Weyl mode. Notably, this is consistent with the Nielsen–Ninomiya theorem [74], which implies, in the one dimensional case, that the number of left movers equals the number of right movers at any energy. In pass we note that, at much higher energy (irrelevant to our purposes), a similar situation occurs: the gap opening up at $ka_0 = \pm\pi$ leaves only two massless helical modes at $E = 4t$, giving rise to one single Dirac cone as low energy excitations around that energy. Only when time-reversal symmetry is present, i.e. for $b = 0$ in equation (C2), the two bands touch at $k = 0$ and $k = \pm\pi$, where an additional Weyl mode appears.

Appendix D. The scattering problem for the inhomogeneous NW with the profile (48)

The solution of the scattering problem for the model (46) with the piecewise constant profile (48) can be obtained from the expression of the electron field operator in the three regions. For an energy E within the magnetic gap ($|E| < E_Z$) one has

$$\hat{\Phi}_E(x) = \begin{cases} \hat{a}_{LE} w_{k_E,-}\, e^{ik_E x} + \hat{b}_{LE} w_{-k_E,-}\, e^{-ik_E x} + \hat{c}_{LE} \tilde{w}_{\kappa_E, s_E}\, e^{\kappa_E x} & x < -L/2 \\ \dfrac{\hat{h}_E}{\sqrt{2}} \begin{pmatrix} 1 \\ 1 \end{pmatrix} e^{ik_{2,E} x} + \dfrac{\hat{g}_E}{\sqrt{2}} \begin{pmatrix} 1 \\ 1 \end{pmatrix} e^{-ik_{2,E} x} + \dfrac{\hat{d}_E}{\sqrt{2}} \begin{pmatrix} 1 \\ -1 \end{pmatrix} e^{\kappa_{2,E} x} + \dfrac{\hat{f}_E}{\sqrt{2}} \begin{pmatrix} 1 \\ -1 \end{pmatrix} e^{-\kappa_{2,E} x} & |x| < L/2 \\ \hat{a}_{RE} w_{-k_E,-}\, e^{-ik_E x} + \hat{b}_{RE} w_{k_E,-}\, e^{ik_E x} + \hat{c}_{RE} \tilde{w}_{-\kappa_E, s_E}\, e^{-\kappa_E x} & x > +L/2 \end{cases}, \tag{D1}$$

where

$$k_E = \frac{\sqrt{2m^*}}{\hbar} \sqrt{E + 2E_{SO} + \sqrt{4EE_{SO} + 4E_{SO}^2 + E_Z^2}} \tag{D2}$$

$$\kappa_E = \frac{\sqrt{2m^*}}{\hbar} \sqrt{-E - 2E_{SO} + \sqrt{4EE_{SO} + 4E_{SO}^2 + E_Z^2}} \tag{D3}$$

$$s_E = \mathrm{sgn}(E + E_Z^2/4E_{SO}) \tag{D4}$$

$$k_{2,E} = k_Z \sqrt{1 + E/E_Z} \qquad \kappa_{2,E} = k_Z \sqrt{1 - E/E_Z}, \tag{D5}$$

while the spinors $w_{\pm k_E,-}$ and $\tilde{w}_{\pm\kappa_E, s_E}$ are given in equations (B5) and (B7), respectively.

Imposing the boundary conditions (47) to the field (D1), one expresses the outgoing operators $\hat{b}_{\mathrm{L/R}E}$ in terms of the operators $\hat{a}_{\mathrm{L}E}$ and $\hat{a}_{\mathrm{R}E}$ describing the modes incoming from the left and from the right region, respectively. The transmission amplitudes t_E and t'_E are then obtained through the relations $\hat{b}_{\mathrm{R}E} = t_E \hat{a}_{\mathrm{L}E}$ and $\hat{b}_{\mathrm{L}E} = t'_E \hat{a}_{\mathrm{R}E}$. The resulting transmission coefficient $T_E = |t_E|^2 = |t'_E|^2$ is numerically exact and is plotted in the solid curves of figure 7 as a function of the spin orbit energy, at the midgap energy $E = 0$ and for different values of the external magnetic field E_Z.

However, as observed in section 4, an analytical expression for the transmission coefficient can be obtained in the low energy limit (dashed curve in figure 7), where the inhomogeneous NW physics is well captured by the effective massless + massive Dirac theory. Such an expression directly follows from the transfer matrix (52) connecting the massless and massive fields of the outer Rashba-dominated regions, which can be obtained as follows. Inserting equation (51) into the low energy boundary conditions equations (49) and (50), the latter can be re-expressed in a matrix form as

$$\mathsf{P}\begin{pmatrix}\hat{\xi}_\uparrow(-L/2)\\ \hat{\xi}_\downarrow(-L/2)\\ \hat{\eta}_\uparrow(-L/2)\\ \eta_\downarrow(-L/2)\end{pmatrix} = \mathsf{V}(-L/2)\begin{pmatrix}\hat{h}\\ \hat{g}\\ \hat{d}\\ \hat{f}\end{pmatrix} \tag{D6}$$

$$\mathsf{V}(L/2)\begin{pmatrix}\hat{h}\\ \hat{g}\\ \hat{d}\\ \hat{f}\end{pmatrix} = \mathsf{Q}\begin{pmatrix}\hat{\xi}_\uparrow(L/2)\\ \hat{\xi}_\downarrow(L/2)\\ \hat{\eta}_\uparrow(L/2)\\ \hat{\eta}_\downarrow(L/2)\end{pmatrix}, \tag{D7}$$

where the energy dependence of the operators has been dropped to make the notation lighter. Here

$$\mathsf{P} = \begin{pmatrix} \mathrm{e}^{-\mathrm{i}k_{\mathrm{SO}}L} & 0 & 1 & 0\\ 0 & \mathrm{e}^{\mathrm{i}k_{\mathrm{SO}}L} & 0 & 1\\ k_{\mathrm{SO}}\,\mathrm{e}^{-\mathrm{i}k_{\mathrm{SO}}L} & 0 & -k_{\mathrm{SO}} & 0\\ 0 & -k_{\mathrm{SO}}\mathrm{e}^{\mathrm{i}k_{\mathrm{SO}}L} & 0 & k_{\mathrm{SO}}\end{pmatrix}, \tag{D8}$$

$$\mathsf{Q} = \begin{pmatrix} \mathrm{e}^{-\mathrm{i}k_{\mathrm{SO}}L} & 0 & 1 & 0\\ 0 & \mathrm{e}^{\mathrm{i}k_{\mathrm{SO}}L} & 0 & 1\\ -k_{\mathrm{SO}}\,\mathrm{e}^{-\mathrm{i}k_{\mathrm{SO}}L} & 0 & k_{\mathrm{SO}} & 0\\ 0 & k_{\mathrm{SO}}\mathrm{e}^{\mathrm{i}k_{\mathrm{SO}}L} & 0 & -k_{\mathrm{SO}}\end{pmatrix} \tag{D9}$$

and

$$\mathsf{V}(x) = \frac{1}{\sqrt{2}} \times \begin{pmatrix} \mathrm{e}^{\mathrm{i}k_{2,E}x} & \mathrm{e}^{-\mathrm{i}k_{2,E}x} & \mathrm{e}^{\kappa_{2,E}x} & \mathrm{e}^{-\kappa_{2,E}x}\\ \mathrm{e}^{\mathrm{i}k_{2,E}x} & \mathrm{e}^{-\mathrm{i}k_{2,E}x} & -\mathrm{e}^{\kappa_{2,E}x} & -\mathrm{e}^{-\kappa_{2,E}x}\\ \mathrm{i}k_{2,E}\,\mathrm{e}^{\mathrm{i}k_{2,E}x} & -\mathrm{i}k_{2,E}\,\mathrm{e}^{-\mathrm{i}k_{2,E}x} & \kappa_{2,E}\,\mathrm{e}^{\kappa_{2,E}x} & -\kappa_{2,E}\,\mathrm{e}^{-\kappa_{2,E}x}\\ \mathrm{i}k_{2,E}\,\mathrm{e}^{\mathrm{i}k_{2,E}x} & -\mathrm{i}k_{2,E}\,\mathrm{e}^{-\mathrm{i}k_{2,E}x} & -\kappa_{2,E}\,\mathrm{e}^{\kappa_{2,E}x} & \kappa_{2,E}\,\mathrm{e}^{-\kappa_{2,E}x}\end{pmatrix}. \tag{D10}$$

The transfer matrix M_E appearing in equation (52) can thus straightforwardly be obtained as $\mathsf{M}_E = \mathsf{Q}^{-1}\mathsf{V}(L/2)\mathsf{V}^{-1}(-L/2)\mathsf{P}$. In particular, setting the energy to the midgap value $E = 0$ and expanding in the parameter $k_Z L$ one obtains equation (53), up to $O((k_Z L)^4)$ terms.

ORCID iDs

Leonid Gogin https://orcid.org/0000-0001-7248-3740
Lorenzo Rossi https://orcid.org/0000-0003-3242-1785
Fausto Rossi https://orcid.org/0000-0001-6729-0928
Fabrizio Dolcini https://orcid.org/0000-0001-9550-9106

References

[1] Geim A K and Novoselov K S 2007 *Nat. Mater.* **6** 183
[2] Castro Neto A H, Guinea F, Peres N M R, Novoselov K S and Geim A K 2009 *Rev. Mod. Phys.* **81** 109
[3] Das Sarma S, Adam S, Hwang E H and Rossi E 2011 *Rev. Mod. Phys.* **83** 407
[4] Hasan M Z and Kane C L 2010 *Rev. Mod. Phys.* **82** 3045
[5] Qi X-L and Zhang S-C 2011 *Rev. Mod. Phys.* **83** 1057
[6] Jia S, Xu S-Y and Hasan M Z 2016 *Nat. Mater.* **15** 1140
[7] Yang S A 2016 *SPIN* **06** 1640003
[8] Takahashi R and Murakami S 2011 *Phys. Rev. Lett.* **107** 166805
[9] Sen D and Deb O 2012 *Phys. Rev.* B **85** 245402

[10] De Beule C and Partoens B 2013 *Phys. Rev.* B **87** 115113
[11] Habe T and Asano Y 2013 *Phys. Rev.* B **88** 155442
[12] Bernevig B A, Hughes T L and Zhang S-C 2006 *Science* **314** 1757
[13] Liu C, Hughes T L, Qi X-L, Wang K and Zhang S-C 2008 *Phys. Rev. Lett.* **100** 236601
[14] König M, Buhmann H, Molenkamp L W, Hughes T, Liu C-X, Qi X-L and Zhang S-C 2008 *J. Phys. Soc. Japan* **77** 031007
[15] Knez I, Du R-R and Sullivan G 2011 *Phys. Rev. Lett.* **107** 136603
[16] Du L, Knez I, Sullivan G and Du R R 2015 *Phys. Rev. Lett.* **114** 096802
[17] Quay C H L, Hughes T L, Sulpizio J A, Pfeiffer L N, Baldwin K W, West K W, Goldhaber-Gordon D and De Picciotto R 2010 *Nat. Phys.* **6** 336
[18] van Weperen I, Plissard S R, Bakkers E P A M, Frolov S M and Kouwenhoven L P 2013 *Nano Lett.* **13** 387
[19] Kammhuber J *et al* 2017 *Nat. Commun.* **8** 478
[20] Mourik V, Zuo K, Frolov S M, Plissard S R, Bakkers E P A M and Kouwenhoven L P 2012 *Science* **336** 1003
[21] Rokhinson L P, Liu X and Furdyna J K 2012 *Nat. Phys.* **8** 795
[22] Das A, Ronen Y, Most Y, Oreg Y, Heiblum M and Shtrikman H 2012 *Nat. Phys.* **8** 887
[23] Deng M T, Yu C L, Huang G Y, Larsson M, Caroff P and Xu H Q 2012 *Nano Lett.* **12** 6414
[24] Lee E J H, Jiang X, Houzet M, Aguado R, Lieber C M and De Franceschi S 2014 *Nat. Nanotechnol.* **9** 79
[25] Albrecht S M, Higginbotham A P, Madsen M, Kuemmeth F, Jespersen T S, Nygård J, Krogstrup P and Marcus C M 2016 *Nature* **531** 206
[26] Deng M T, Vaitiekėnas S, Hansen E B, Danon J, Leijnse M, Flensberg K, Nygård J, Krogstrup P and Marcus C M 2016 *Science* **354** 1557
[27] Önder G *et al* 2018 *Nat. Nanotech.* **13** 192
[28] Středa P and Šeba P 2003 *Phys. Rev. Lett.* **90** 256601
[29] Oreg Y, Refael G and von Oppen F 2010 *Phys. Rev. Lett.* **105** 177002
[30] Lutchyn R M, Sau J D and Das Sarma S 2010 *Phys. Rev. Lett.* **105** 077001
[31] Kloeffel C, Trif M and Loss D 2011 *Phys. Rev.* B **84** 195314
[32] Cheng M and Lutchyn R M 2012 *Phys. Rev.* B **86** 134522
[33] Szumniak P, Chevallier D, Loss D and Klinovaja J 2017 *Phys. Rev.* B **96** 041401
[34] Kitaev A Y 2001 *Phys.-Usp.* **44** 131
[35] Alicea J 2012 *Rep. Prog. Phys.* **75** 076501
[36] Sato M and Fujimoto S 2016 *J. Phys. Soc. Japan* **85** 072001
[37] Aguado R 2017 *La Rivista del Nuovo Cimento* **40** 523
[38] Sasaki S, Tateno K, Zhang G, Suominen H, Harada Y, Saito S, Fujiwara A, Sogawa T and Muraki K 2013 *Appl. Phys. Lett.* **103** 213502
[39] Burke A M, Carrad D J, Gluschke J G, Storm K, Fahlvik Svensson S, Linke H, Samuelson L and Micolich A P 2015 *Nano Lett.* **15** 2836
[40] Takase K, Ashikawa Y, Zhang G, Tateno K and Sasaki S 2017 *Sci. Rep.* **7** 930
[41] Das S R 2019 *Nanoelectronics: Devices, Circuits and Systems* ed B K Kaushik (Amsterdam: Elsevier) ch 11 p 355
[42] Yin Y, Zhang Z, Zhong H, Shao C, Wan X, Zhang C, Robertson J and Guo Y 2021 *ACS Appl. Mater. Interfaces* **13** 3387
[43] Takase K, Tateno K and Sasaki S 2021 *Appl. Phys. Lett.* **119** 013102
[44] Liang D and Gao X P A 2012 *Nano Lett.* **12** 3263
[45] Slomski B, Landolt G, Muff S, Meier F, Osterwalder J and Dil J H 2013 *New J. Phys.* **15** 125031
[46] van Weperen I, Tarasinski B, Eeltink D, Pribiag V S, Plissard S R, Bakkers E P A M, Kouwenhoven L P and Wimmer M 2015 *Phys. Rev.* B **91** 201413
[47] Scherübl Z, Fülöp G, Madsen M H, Nygård J and Csonka S 2016 *Phys. Rev.* B **94** 035444
[48] Bindel J R, Pezzotta M, Ulrich J, Liebmann M, Sherman E Y and Morgenstern M 2016 *Nat. Phys.* **12** 920
[49] Borge J and Tokatly I V 2017 *Phys. Rev.* B **96** 115445
[50] Kloeffel C, Rančić M J and Loss D 2018 *Phys. Rev.* B **97** 235422
[51] Wójcik P, Bertoni A and Goldoni G 2018 *Phys. Rev.* B **97** 165401
[52] Tsai H, Karube S, Kondou K, Yamaguchi N, Ishii F and Otani Y 2018 *Sci. Rep.* **8** 5564
[53] Premasiri K and Gao X P A 2019 *J. Phys.: Condens. Matter.* **31** 193001
[54] Shcherbakov D *et al* 2021 *Sci. Adv.* **7** eabe2892
[55] Krupin O, Bihlmayer G, Starke K, Gorovikov S, Prieto J E, Döbrich K, Blügel S and Kaindl G 2005 *Phys. Rev.* B **71** 201403
[56] Wang W, Li X M and Fu J Y 2016 *J. Magn. Magn. Mater.* **411** 84
[57] Nagasawa F, Reynoso A A, Baltanás J P, Frustaglia D, Saarikoski H and Nitta J 2018 *Phys. Rev.* B **98** 245301
[58] Peres N M R 2009 *J. Phys.: Condens. Matter.* **21** 095501
[59] Nilsson H A, Caroff P, Thelander C, Larsson M, Wagner J B, Wernersson L-E, Samuelson L and Xu H Q 2009 *Nano Lett.* **9** 3151
[60] Nadj-Perge S, Pribiag V S, van den Berg J W G, Zuo K, Plissard S R, Bakkers E P A M, Frolov S M and Kouwenhoven L P 2012 *Phys. Rev. Lett.* **108** 166801
[61] Roulleau P, Choi T, Riedi S, Heinzel T, Shorubalko I, Ihn T and Ensslin K 2010 *Phys. Rev.* B **81** 155449
[62] Joyce H J, Docherty C J, Gao Q, Tan H H, Jagadish C, Lloyd-Hughes J, Herz L M and Johnston M B 2013 *Nanotechnology* **24** 214006
[63] Sánchez D and Serra L 2006 *Phys. Rev.* B **74** 153313
[64] Sánchez D, Serra L and Choi M-S 2008 *Phys. Rev.* B **77** 035315
[65] Glazov M M and Sherman E Y 2011 *Phys. Rev. Lett.* **107** 156602
[66] Sadreev A F and Sherman E Y 2013 *Phys. Rev.* B **88** 115302
[67] Modugno M, Sherman E Y and Konotop V V 2017 *Phys. Rev.* A **95** 063620
[68] Klinovaja J and Loss D 2015 *Eur. Phys. J.* B **88** 62
[69] Dolcini F and Rossi F 2018 *Phys. Rev.* B **98** 045436
[70] Rossi L, Dolcini F and Rossi F 2020 *Phys. Rev.* B **101** 195421
[71] Rossi L, Dolcini F and Rossi F 2020 *Eur. Phys. J. Plus* **135** 597
[72] Datta S 1995 *Electronic Transport in Mesoscopic Systems* (Cambridge: Cambridge University Press)
[73] Dolcini F, Iotti R C, Montorsi A and Rossi F 2016 *Phys. Rev.* B **94** 165412
[74] Nielsen H B and Ninomiya M 1981 *Nucl. Phys.* B **193** 173